Heliyon 10 (2024) e26709

Contents lists available at ScienceDirect

Heliyon

journal homepage: www.cell.com/heliyon

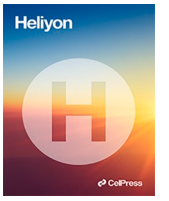

Research article

A theoretical and electrochemical impedance spectroscopy study of the adsorption and sensing of selected metal ions by 4-morpholino-7-nitrobenzofuran

Imen Chérif [a,b], Bouzid Gassoumi [c], Hajer Ayachi [d], Mosaab Echabaane [e], Maria Teresa Caccamo [b], Salvatore Magazù [b], Ayoub Haj Said [c], Boubaker Taoufik [d], Sahbi Ayachi [a,*]

[a] *Laboratory of Physico-Chemistry of Materials (LR01ES19), Faculty of Sciences, Avenue of the Environment 5019 Monastir, University of Monastir, Tunisia*
[b] *Dipartimento di Scienze Matematiche e Informatiche, Scienze Fisiche e Scienze della Terra, Università di Messina, Viale Ferdinando Stagno D'Alcontres No. 31, S. Agata, 98166, Messina, Italy*
[c] *Laboratoire Interfaces et Matériaux Avancés (LIMA), Faculté des Sciences, Université de Monastir, Avenue de l'Environnement, 5019, Monastir, Tunisia*
[d] *Laboratoire de Chimie Hétérocyclique, Produits Naturels et Réactivité (LR11ES39), Faculté des Sciences, Université de Monastir, Avenue de l'Environnement, 5019, Monastir, Tunisia*
[e] *CRMN, Centre de Recherche en Microélectronique et Nanotechnologie de Sousse, Nanomisene, LR16CRMN01, 4054, Sousse, Tunisie*

ARTICLE INFO

Keywords:
Nitrobenzofurazan
Heavy metals
FT-IR/^{1}H NMR spectroscopy
DFT
Reactivity and selectivity
Electronic charge transfer
QTAIM

ABSTRACT

The selectivity of a novel chemosensor, based on a modified nitrobenzofurazan referred to as NBD-Morph, has been investigated for the detection of heavy metal cations (Co^{2+}, Pb^{2+}, Mg^{2+}, Ag^{+}, Cu^{2+}, Hg^{2+}, Ni2+, and Zn^{2+}). The ligand, 4-morpholino-7-nitrobenzofurazan (NBD-Morph), was characterized using spectroscopic techniques including FT-IR and ^{1}H NMR. Vibrational frequencies obtained from FT-IR and proton NMR (^{1}H) chemical shifts were accurately predicted employing the density functional theory (DFT) at the B3LYP level of theory. Furthermore, an examination of the structural, electronic, and quantum chemical properties was conducted and discussed. DFT calculations were employed to explore the complex formation ability of the NBD-Morph ligand with Co^{2+}, Pb^{2+}, Mg^{2+}, Ag^{+}, Cu^{2+}, Hg^{2+}, Ni^{2+}, and Zn^{2+} metal cations. The comparison of adsorption energies for all possible conformations reveals that NBD-Morph exhibits sensitivity and selectivity towards metal ions, including Pb^{2+}, Cu^{2+}, Ag^{+}, and Ni^{2+}. However, an assessment of their reactivity using QTAIM topological parameters demonstrated the ligand's greater complexation ability toward Cu^{2+} or Ni^{2+} than those formed by Pb^{2+} or Ag^{+}. Additionally, molecular electrostatic potential (MEP), Hirshfeld surfaces, and their associated 2D-fingerprint plots were applied to a detailed study of the inter-molecular interactions in NBD-Morph-X (X = Pb^{2+}, Cu^{2+}, Ag^{+}, Ni^{2+}) complexes. The electron localization function (ELF) and the localized-orbital locator (LOL) were generated to investigate the charge transfer and donor-acceptor interactions within the complexes. Electrochemical analysis further corroborates the theoretical findings, supporting the prediction of NBD-Morph's sensory ability towards Ni^{2+} metal cations. In conclusion, NBD-Morph stands out as a promising sensor for Ni^{2+}.

* Corresponding author.
E-mail address: ayachi_sahbi@yahoo.fr (S. Ayachi).

https://doi.org/10.1016/j.heliyon.2024.e26709
Received 7 September 2023; Received in revised form 16 February 2024; Accepted 19 February 2024
Available online 23 February 2024

1. Introduction

The presence of harmful heavy metals, including cobalt (Co), lead (Pb), magnesium (Mg), silver (Ag), copper (Cu), mercury (Hg), nickel (Ni), and zinc (Zn), in industrial wastewater constitutes a significant environmental issue due to contamination [1]. Heavy metal pollution is a common form of pollution that has long-lasting effects and is difficult to remove due to its persistence. This contamination is exacerbated by organic matter cycles and energy flows, causing the migration and accumulation of heavy metals through the food chain, posing a hazard to human health [2].

The scientific community is increasingly interested in the use of adsorbents obtained from biomass to eliminate these metals [3,4]. Heavy metals are well-known environmental pollutants due to their toxicity, persistence, and bio-accumulative nature [5]. Numerous techniques have been developed to eliminate these metals from water, for instance, precipitation, solvent extraction, and ion exchange. However, adsorption is the most frequently utilized approach due to its versatility, efficiency, accuracy, and ease [1,4,6,7]. The quest for economically beneficial and readily accessible adsorbents has prompted the investigation of bioactive polymers as potential alternatives in this domain. Among the numerous adsorbents available for heavy metal adsorption, cellulose, chitosan, synthetic polymers, organic and inorganic molecules are commonly employed [8–10].

4-Nitrobenzofurazan (NBD) is a neutral 10 π electron-deficient hetero-aromatic substrate. The inclusion of NBD in organic materials has been studied for potential applications in biomedical and bio-analytical fields [11–17]. The electron-donating and electron-withdrawing groups play a significant role in determining the ICT extent in super-electrophiles containing methoxyl or phenoxyl at the para-position, as strong electron-donating groups [18]. S_NAr reactions using NBD chloride (NBD-Cl) and similar compounds are initiated by nucleophilic groups such as morpholine, piperidine, or pyrrolidine, secondary amines, affording the formation of new NBD derivatives with unique UV–vis optical absorption properties in polar solvents [19,20]. Alternatively, NBD derivatives have been utilized as key components in organic photovoltaic materials due to their effective electron-withdrawing and donating properties [21]. The NBD derivatives are highly efficient for adsorbing heavy metals due to a combination of unique properties. They possess high selectivity, allowing for efficient removal of specific metals from contaminated water [22]. They also have a large surface area with multiple functional groups, providing more active sites for metal adsorption. Additionally, their water solubility enables easy preparation of adsorbent solutions and effective mixing with contaminated water [23]. NBD derivatives are stable and resistant to degradation, making them suitable for long-term heavy metal adsorption applications [24]. Moreover, they can be regenerated and reused after adsorbing heavy metals, making them an economically viable option for heavy metal removal.

The pollution of the environment by heavy metals is a major concern due to their toxic effects on living organisms. Therefore, understanding the interaction of heavy metals with receptors is crucial for developing effective remediation strategies [25–31]. Within this framework, the spectroscopic analysis and binding interaction of heavy metals onto the surface receptor of NBD-Morph have been investigated using a combination of DFT and experimental approaches. The aim of this work is to develop a comprehensive background for understanding the binding mechanism of heavy metals with the surface receptor, elucidated by spectroscopic techniques and computational modeling. Efforts are being made to develop effective methods for eliminating heavy metals from the environment.

2. Synthesis procedure

By applying nucleophilic aromatic substitution reaction (S_NAr), 4-chloro-7-nitrobenzofurazan (NBD-Cl; Fluka BioChemika), used as received, was utilized as the electrophile and reacted with morpholine, as the nucleophilic reagent, to yield the final product, named NBD-Morph [32–35]. The substitution product (NBD-Morph) was prepared as follows: 3g (15 mmol) of NBD-Cl and 1.3 mL (15 mmol) of morpholine were dissolved in 50 mL of acetonitrile, and the mixture was heated to 40 °C. After 20 min, a yellow precipitate began to form. The crystals deposited after 40 min were filtered, thoroughly washed with water, and dried under vacuum. NBD-Morph was thus obtained in an 80% yield with a melting point of 175 °C (see Scheme 1).

3. Materials and methods

3.1. Preparation of electrode

It is crucial to clean the platinum working electrode before each electrochemical measurement. Prior to any modification, the

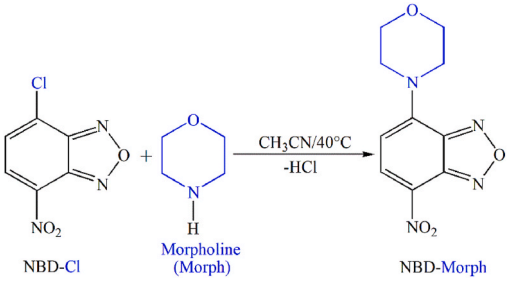

Scheme 1. S_NAr mechanism of NBD-Cl with morpholine in acetonitrile.

electrode underwent a successful cleaning process in an ultrasonic bath containing acetone and isopropanol for 10 min. Following each cleaning step, thorough rinsing with deionized water was carried out, and the electrode was then dried at room temperature in an oven. To functionalize the electrode, aqueous solutions of NBD-Morph were prepared by dissolving 1 mg in 1 mL of water. Subsequently, using the drop-casting method, 3 μL of NBD-Morph solution was applied to the working electrode (WE) area and allowed to dray at 60 °C for 60 min to prepare it for electrochemical measurements.

3.2. Electrochemical measurements

Using Autolab PGSTAT30, supported by the software installed in a "FRA2″ computer, electrochemical impedance spectroscopy (EIS) measurements were conducted. A sinusoidal excitation signal with an amplitude of 10 mV was applied for these measurements, covering frequencies ranging from 30 mHz to 100 kHz in the impedance spectra. The optimal potential was determined to be −0.9 V. The electrochemical cell consisted of a 0.1 M ammonium acetate solution with a pH of 7, three electrodes (a working electrode (WE) made of platinum (Pt), a counter-electrode made of platinum, and a saturated calomel reference electrode). It is worth noting that the EIS measurements were performed on three electrodes. The module of impedance (|Z|) at 1 Hz was used to estimate the sensor's response. Experimental data were then subjected to fitting using the ZView software.

3.3. NMR and FT-IR measurement

A proton nuclear magnetic resonance structural study was recorded at 500 MHz in deuterated chloroform on a Bruker AC 500 spectrometer for NBD-Morph, and chemical shifts (δ) are reported in ppm relative to tetramethylsilane (TMS; $\delta = 0$), as an internal reference.

The PerkinElmer FT-IR was employed to record the FT-IR spectra of the material under study in a KBr pellet at room temperature. The spectral range for the sample was from 400 cm^{-1} to 4000 cm^{-1}, with a spectral resolution of 0.5 cm^{-1}.

3.4. Computational methods

Recently, the hybrid functional B3LYP has been used to perform calculations on NBD derivatives. Consequently, some electrochemical and photo-physical properties have been accurately predicted in previous studies [19,36–39]. In line with these advancements, we have adopted the same approach to explore the properties of the materials under investigation.

The optimized geometry of the NBD-Morph molecule was achieved using the Gaussian 09 software [40]. Full calculations were performed in polar acetonitrile (CH_3CN) and water by implementing the conductor-like polarizable continuum model (CPCM) [41–43] and the B3LYP (Becke three-parameter Lee-Yang-Parr) exchange-correlation functional DFT [44,45], utilizing the 6–31+g(d,p) and LanL2DZ basis sets. Meanwhile, the LanL2DZ basis set was investigated for complexation with Co^{2+}, Pb^{2+}, Mg^{2+}, Ag^{+}, Cu^{2+}, Hg^{2+}, Ni^{2+}, and Zn^{2+}.

To compute ^{1}H NMR chemical shifts, the Gauge-Independent Atomic Orbital (GIAO) [46] method was applied. DFT/B3LYP/6–31+g(d,p) level of theory was also employed to determine the vibrational frequencies of the title compound. For the vibrational analysis, the FT-IR spectrum has been registered in the range of 400–4000 cm^{-1}. The calculated normal mode vibrational frequencies and the TED (%) values were analyzed within the VEDA software [47].

In addition, various global reactivity parameters were determined based on the frontier molecular orbitals (FMOs). The HOMO and LUMO energy levels, the electronic gap energy (Eg), chemical potential (μ), global hardness (η), and global softness (σ) are determined and expressed through the subsequent formulas [48–50]:

$$Eg = E_{LUMO} - E_{HOMO} \quad \text{Eq. (1)}$$

$$\mu = (E_{HOMO} + E_{LUMO}) / 2 \quad \text{Eq. (2)}$$

$$\eta = (E_{LUMO} - E_{HOMO}) / 2 \quad \text{Eq. (3)}$$

$$\sigma = 1 / \eta \quad \text{Eq. (4)}$$

Moreover, we have computed the adsorption energy at the DFT/B3LYP/LanL2DZ level of theory in water using the equation given below:

$$E_{Ad/Solv} = E_{Complex} - (E_{Molecule} + E_{Cation}) + E_{BSSE} \quad \text{Eq. (5)}$$

Where:

$E_{Complex}$: The total energy of cations adsorbed on the NBD-Morph.

$E_{Molecule}$: The total energy of an isolated NBD-Morph.

E_{cation}: The total energy of isolated cations (Co^{2+}, Pb^{2+}, Mg^{2+}, Ag^{+}, Cu^{2+}, Hg^{2+}, Ni^{2+}, Zn^{2+}).

E_{BSSE}: The counterpoise approach, which was employed to correct the Basis Set Superposition Error [51].

The Crystal Explorer 17.5 program [52] was used to produce the Hirshfeld (HS) surface analysis. Additionally, ELF and LOL analyses were carried out using the software multiwfn_3.7 [53].

4. Results and discussion

4.1. Ground-state (S_0) optimized structure of the studied ligand

The DFT/B3LYP method was utilized to examine the structural parameters of NBD-Morph in gas state and in two distinct solvents, water or acetonitrile, using the 6–31+g(d,p) and LanL2DZ basis sets. The objective was to define the most stable geometry in the most appropriate solvent and basis set. The optimized structure of NBD-Morph with atomic numbering is depicted in Fig. 1. The calculated values are summarized in Table 1**.** It can be clearly seen that the highest values for both basis sets were found using water as the solvent. In this section, all calculations were performed in the solvent water. Their corresponding energy and dipole moment at DFT/B3LYP/6–31+g(d,p) and DFT/B3LYP/LanL2DZ were found to be −906.842832/-906.6488849 Hartree and 13.7320/15.2360 Debye, respectively.

The conformer exhibiting low energy has been selected for subsequent optimization by the use of the B3LYP hybrid functional at 6–31+g(d,p) and LanL2DZ basis sets. Table 2 presents the NBD-Morph molecule's structural characteristics, such as bond lengths, bond angles, and torsion angles, which have been compared to those previously reported for analogous compounds [54,55].

Based on the structural information presented in Tables 2 and it is clear that the experimental results are consistent with theoretical predictions obtained at the B3LYP/6–31+g(d,p) level of theory. Interestingly, the optimized bond lengths of C3–C4, C3–N13, C5–C4, C6–H20, N15–O14, O14–N13, N16–O17, and N16–O18 are in close proximity to the experimental measurements. Likewise, it is found that some of the bond angles closely match the experimental values, which are present with C5–C4–N15, O17–N16–O18, O17–N16–C2, C5–C6–H20, and C2–C3–N13. It is clear to state that most of the computed bond lengths and bond angle values are slightly larger than the experimental ones. This difference can be explained by the fact that H-bonding interactions within the solid phase are not taken into account in the calculation [56,57]. According to Table 2, most of the calculated values are consistent with theoretical and experimental values from the literature.

Mapping the molecular electrostatic potential (MEP) is an extremely valuable technique for examining the nucleophilic and electrophilic characteristics of the compound under investigation [58–61]. The MEP method has proven to be a fitting approach for determining the three-dimensional charge distributions of molecules. This is achieved by utilizing the optimized geometry at the B3LYP/LanL2DZ level of theory. As depicted in Fig. 2, red negative regions are related to electrophilic reactivity, and blue positive regions are ascribed to nucleophilic sites. Color-coded maps of the NBD-Morph were generated within the limits of 0.0460 a.u. and 0.0460 a.u. MEP is among the best tools for determining intra- and inter-molecular interaction sites [62].

The MEP map reveals the negative area around the oxygen atoms (O_{10}, O_{14}, $O_{17,}$ and O_{18}). The most negative potential region (red) is present around O_{17} and O_{18}, which are linked with nitrogen atoms through a double bond (N_{16}═O_{18}) and a simple bond (N_{16}–O_{17}). Moreover, the positive MEP results are on hydrogen atoms of NBD-Morph. Regions of reduced electron density, namely σ-holes and π-holes, are commonly present in molecules. These regions often exhibit positive electrostatic potentials, facilitating attractive interactions with negative sites and leading to the formation of noncovalent bonds.

4.2. NMR spectral analysis

NMR spectroscopy is an extremely suitable tool for the structural analysis of organic systems. The calculated and recorded ^{1}H chemical shifts in deuterated chloroform ($CDCl_3$) solution relative to tetramethylsilane (TMS) are given in Table 3. The computed and experimental ^{1}H NMR spectra of the NBD-Morph ligand are illustrated in Figs. 3 and 4, respectively, for comparison. Note that all the chemical shifts are indexed with respect to the numbered atoms provided in Fig. 1**.** Consequently, the two aromatic protons (H_{19} and H_{20}) of the studied compound exhibit double resonances within the range of 8.39 ppm and 6.27 ppm (vs. 8.93 ppm and 6.72 ppm) for the experimental spectrum (vs. the theoretical spectrum).

Due to the presence of the nitro group (NO_2) in the ortho-position of this hydrogen atom, the H19 proton had a higher unshielded signal than the H20 proton. Due to the strong electron delocalization in the benzene ring, these protons resonate at a slightly lower

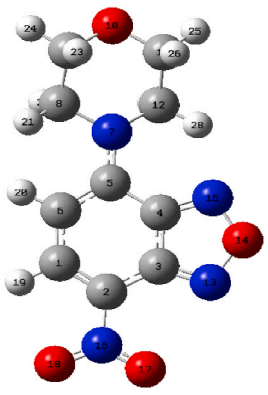

Fig. 1. The stable structure of NBD-Morph with atomic numbering.

Table 1
DFT/B3LYP/6–31+g(d,p) and LanL2DZ methods used to separately calculate the electronic and quantum chemical parameters for the NBD-Morph in water and in acetonitrile.

	DFT/B3LYP/6–31+g(d,p)			DFT/B3LYP/LanL2DZ		
	Water	Acetonitrile	Gas	Water	Acetonitrile	Gas
E_T (a.u)	−906.84283	−906.84234	−906.82116	−906.64888	−906.64826	−906.62053
E_g (eV)	3.048	3.053	3.290	2.835	2.837	3.016
E_{HOMO} (eV)	−6.344	−6.349	−6.661	−6.372	−6.375	−6.669
E_{LUMO} (eV)	−3.956	−3.296	−3.3707	−3.536	−3.537	−3.653
μ (eV)	−4.819	−4.822	−5.016	−4.954	−4.956	−5.161
η (eV)	1.524	1.526	1.645	1.417	1.418	1.508
S (eV^{-1})	0.3280	0.327	0.304	0.352	0.352	0.331
μ_D (Debye)	13.732	13.577	8.409	15.236	15.093	9.518

Table 2
Calculated and experimental structural parameters of the NBD-Morph compound have been calculated. The bond lengths (Å), bond angles, and dihedral angles (°), were calculated by the DFT/B3LYP/6–31+g(d,p) and DFT/B3LYP/LanL2DZ levels of theory.

Bond Length (Å)	6-31+g(d,p)	LanL2DZ	[a]Litera.	Bond Angles (°)	6-31+g(d,p)	LanL2DZ	[a]Litera.
C1–C2	1.377	1.391	1.545	C1–C2–C3	117.2	117.6	108.2
C1–C6	1.412	1.414	1.508	C1–C6–C5	123.09	123.05	121.0
C1–H19	1.084	1.085	1.006	C3–C5–C5	122.6	122.5	120.6
C2–C3	1.429	1.431	1.496	C3–C4–N15	108.1	109.2	109.3
C2–N16	1.446	1.448	1.544	C2–C3–N13	131.0	131.9	129.9
C3–N13	1.322	1.350	1.289	C3–N13–O14	104.6	103.7	104.9
C3–C4	1.445	1.461	1.425	C4–C3–C2	119.4	119.1	120.4
C4–C5	1.455	1.461	1.439	C4–C5–C6	113.2	114.3	119.91
C4–N15	1.320	1.344	1.297	C4–C5–N7	122.1	122.4	–
C5–C6	1.399	1.413	1.320	C5–C4–N15	129.1	128.2	130.1
C5–N7	1.370	1.376	–	C2–C1–H19	117.6	117.4	102.0
C6–H20	1.081	1.082	1.115	C6–C1–H19	119.01	119.3	114.0
N7–C12	1.477	1.491	–	C1–C6–H20	116.92	116.95	117.1
N7–C8	1.467	1.483	–	C5–C6–H20	119.9	119.9	120.7
C8–C9	1.530	1.542	–	N15–O14–N13	112.7	112.9	104.6
C9–O10	1.418	1.456	–	O17–N16–O18	124.6	123.7	125.1
O10–C11	1.423	1.462	–	O17–N16–C2	117.4	118.2	117.9
C11–C12	1.524	1.535	–	O18–N16–C2	117.8	118.0	117.0
N15–O14	1.358	1.409	1.384	C6–C5–N7	123.5	123.3	–
O14–N13	1.372	1.438	1.380	C8–N7–C12	112.77	112.72	–
N16–O17	1.232	1.281	1.216	N7–C12–C11	110.4	110.7	–
N16–O18	1.238	1.288	1.202	C12–C11–O10	111.3	110.7	–
N16–C2	1.446	1.448	1.544	C9–O10–C11	110.3	110.3	–

[a] Taken from Ref. [51,54].

field than those cited in the literature [63]. The aromatic ring protons detected in this range are attributed to a potent ICT that involves the thoroughly examined molecule. In fact, this is due to the effect of the nitro group on the ^{1}H chemical shifts of benzene, which will be influenced by the inductive, resonance, and magnetic anisotropy effects [64]. H23, H24, H25, and H26 resonance signals were easily assigned. The shielded signals of these four protons appear as a singlet resonance in the 4.02 ppm range. As can be clearly seen, the computed ^{1}H NMR shifts provide a satisfactory prediction of the measured data. Ultimately, the use of the DFT approach gives useful insights into the structural characteristics of the investigated title compound.

It is interesting to note that the high δ_{Theo} theoretical value of 5.79 ppm is due to the presence of an intramolecular hydrogen bond between H_{28} and the nitrogen atom of the NBD ring.

4.3. Infrared vibrational analysis

Initially, the experimental identification of characteristic functional groups in the examined NBD-Morph compound was achieved through a detailed analysis of its infrared (IR) spectrum (see Fig. 5 and Table 4). The stretching bands indicative of various bonds, including but not limited to C–O, C–N, NO_2, C═N, and aliphatic C–H bending, were carefully examined. Assigning these peaks serves as a crucial tool for elucidating the formation of the NBD-Morph product. Table 4 summarizes the prominent peaks and their respective functional groups in the studied NBD-Morph compound.

To provide additional support for the ligand's chemical structure, structural information about the material can be elucidated theoretically. Here, we have calculated the infrared (IR) vibrational spectrum and determined the corresponding vibrational frequencies, which are then compared to those measured. The DFT/B3LYP/6–31+g(d,p) method has been applied to simulate the IR spectrum of the investigated compound. The obtained results were further analyzed via VEDA software [47]. For each normal mode,

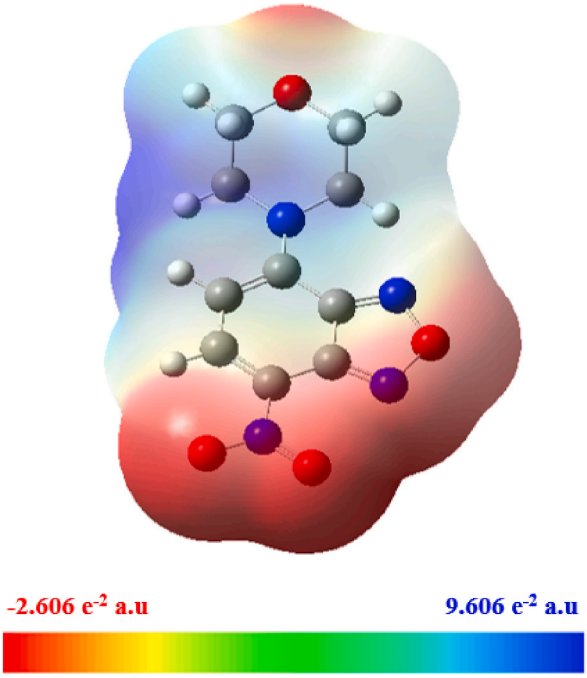

Fig. 2. The MEP plot of NBD-Morph at the DFT/B3LYP/LanL2DZ level of theory.

Table 3
Experimental and computed ^{1}H NMR chemical shifts for the NBD-Morph ligand.

Atom	δ_{Exp} (ppm)	δ_{Theo} (ppm)
H_{19}	8.39	8.93
H_{20}	6.27	6.72
H_{21}	3.89	3.60
H_{22}		3.64
H_{27}		3.62
H_{28}		5.79
H_{23}	4.02	4.13
H_{24}		4.34
H_{25}		4.31
H_{26}		4.27

the total energy distribution (TED) among the symmetry coordinates of the molecules was computed. Thus, a complete vibrational assignment of the fundamental modes was proposed based on the calculated TED values and IR intensities. The animation option of Gauss View 06 allows us to visualize the different IR vibration modes resulting from the simulated spectrum. The IR absorption spectra, characteristic of both theoretical and experimental molecular vibrations of the NBD-Morph compound, are given in Fig. 5. Experimentally observed IR bands, calculated frequencies, and their assignments are shown in Table 5. It is evident that performing DFT calculations yields a simulated spectrum that closely corresponds to the experimental one.

The FT-IR spectra of NBD-Morph exhibited optical bands with their respective shifts due to the presence of multiple bonds. The studied molecule exhibits typical C–H vibrations and aromatic C–C vibrations. This type of vibration occurs when one or more rings that are more aromatic are present in the molecular structure. This can be easily determined from the stretching vibrations of the C–H and C–C rings. The C–H stretching vibration is typically observed at frequencies higher than 3000 cm^{-1} and is often observed as a band with low to moderate intensity when compared to the stretching aliphatic C–H bonds [65]. Here, the C–H stretching vibration of the Benzofurazn ring is found in the IR spectrum at 3227 cm^{-1}. By using the B3LYP/6–31+g(d,p) level of theory, the same vibration is computed at 3237 cm^{-1}. Then, we observed a good agreement between the computed value and the measured data. As shown in the TED values, this mode (mode 26) implies an exact contribution of 96%, which suggests that it is a pure stretching mode. We find that the aromatic C–H stretching bonds are weakened by the decrease in dipole moment due to the reduction of the negative charge on the carbon atom.

The C–H in-plane-bending vibration usually appears within the 1050-1520 cm^{-1} range [46]. Here, the observed peaks of absorption in the FT-IR spectrum between 1193 cm^{-1} and 1597 cm^{-1} were associated with the C–H in plane bending vibrations. The computed vibrational frequencies for the C–H in plane bending vibrations were within the range of 1195–1589 cm^{-1}, showing

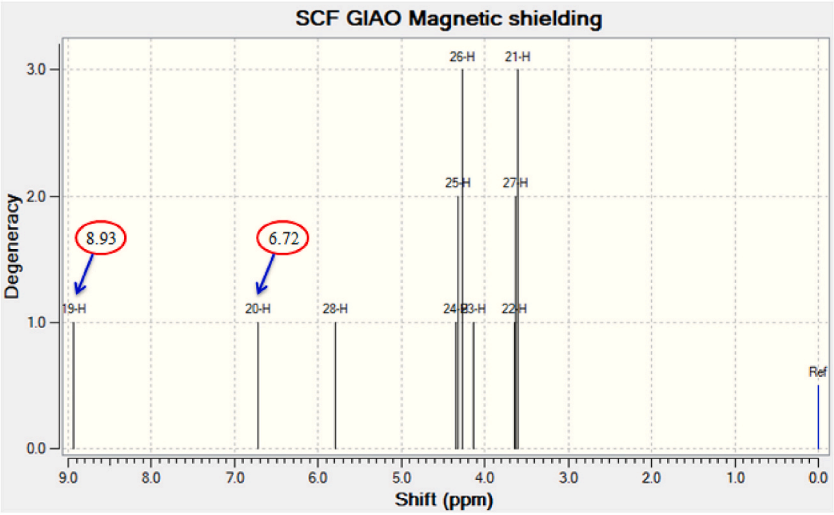

Fig. 3. Theoretical ^{1}H NMR spectrum of NBD-Morph.

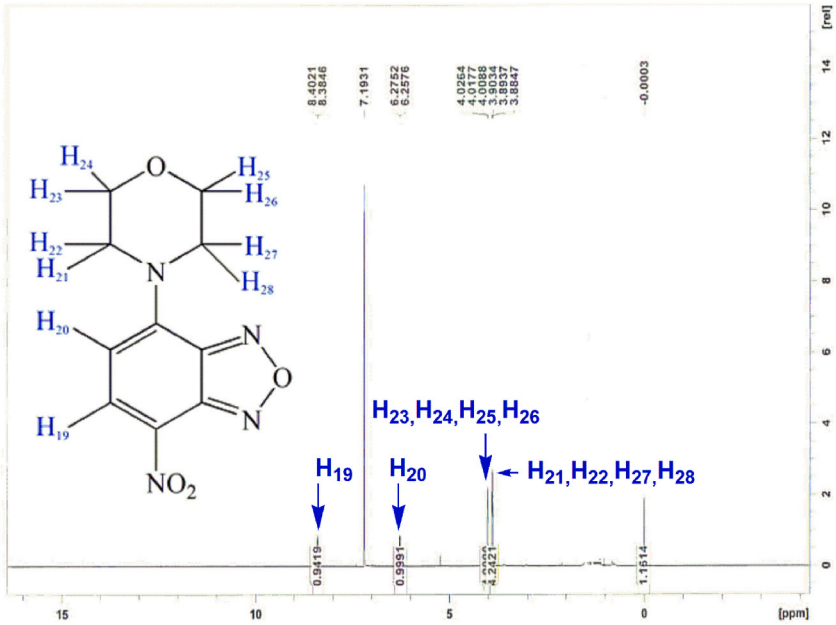

Fig. 4. Experimental ^{1}H NMR spectrum of the NBD-Morph.

significant agreement with the experimental results. The IR-active C–H in-plane bending mode of the NBD-Morph appears at 1482 cm^{-1}, exhibiting a pronounced TED contribution of 62%. Most of the computed vibrational frequencies are assigned to C═C and C–C stretching modes, in good agreement with the experiment results.

The range between 1200 and 1650 cm^{-1} is predicted for the phenyl group's carbon-carbon stretching modes. According to Ref. [46], the vibrations related to the stretching of C–C bonds are estimated to occur between the ranges of 800 and 1700 cm^{-1}. Generally, the characteristics of the substitutes [66] do not significantly alter these frequencies, which are crucial and distinctly associated with the aromatic ring itself.

The IR C–C stretching vibration bands were found around 611, 830, 1027, 1597, and 1643 cm^{-1} with a significant contribution from TED. Hence, the FT-IR bands observed at 733 and 905 cm^{-1} in the title compound have been assigned to C–C–C in plane bending vibrations. These vibrational frequencies are comparable to those previously reported in the literature for these groups [67]. Typically, it is extremely difficult to differentiate between the C–N and C═N vibrations due to the possibility of multiple bands overlapping in this spectral region [68]. The C–N stretching vibration is typically observed at 1307 and 1382 cm^{-1} for benzotriazole, while for benzamid, the stretching of the C–N bond is detected at 1368 cm^{-1} [69].

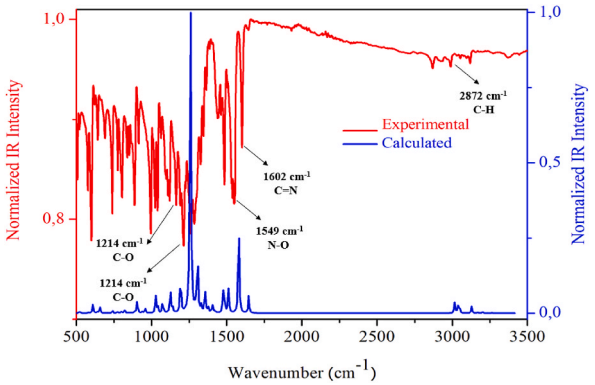

Fig. 5. Experimental and calculated FT-IR spectra for the NBD-Morph.

Table 4
Prominent peaks and their respective functional groups in the NBD-Morph studied compound.

Groups	Appearance	Frequency (cm^{-1})
C–O Stretching	strong	1214
C–N Stretching	medium	1203
C═N Stretching	medium	1602
NO_2 Stretching	Strong	1549
Aliphatic C–H Stretching	Weak, broad	2872

Table 5
Experimental and computed vibrational frequencies (cm^{-1}).

THO	EXP	Vibration *+TED (≥10%)
608	611	*C1C2* ***STRE(19)*** + *C2C3* ***STRE(15)*** + *C4N15O14N13* ***TORS(66)*** + *N7C4C6C5* ***oop(13)***
658	646	*N7C4C6C5* ***oop (30)*** + *C8C12C5N7* ***oop (14)*** + *C3N13O14N15* ***TORS (23)***
739	733	*C6C1C2* ***BEND (12)***
745	744	*O18C2O17N16* ***oop (75)***
770	773	*C1C2C3C4* ***TORS(18)*** + *C3N13O14N15* ***TORS(16)*** + *C4N15O4N13* ***TORS (16)*** + *N7C4C6C5* ***oop(13)*** + *O18C2O17N16* ***oop(10)***
821	830	*O14N13* ***STRE(58)*** + *O10C11* ***STRE(28)*** + *N7C12* ***STRE(18)*** + *C11C12* ***STRE(12)*** + *H20C6C5N7* ***TORS(66)*** + *H19C1C6C* ***TORS(13)***
908	905	*O10C9* ***STRE(11)*** + *N7C8* ***STRE(11)*** + *O10C11* ***STRE(11)*** + *O14N13* ***STRE(11)*** + *C5C6C1* ***BEND(10)***
958	992	*O14C9* ***STRE(57)*** + *N13O14N15* ***BEND(19)*** + *O10C11C12* ***BEND(14)*** + *C11C12N7* ***BEND(14)*** + *H19C1C6C5* ***TORS(58)***
1026	1027	*C11C12* ***STRE(34)*** + *O14N15* ***STRE(11)*** + *N16C2* ***STRE(10)*** + *N7C8* ***STRE(10)*** + *C9O10C11* ***BEND(12)*** + *N13O14N15* ***BEND(17)***
1071	1084	*O14N15* ***STRE(10)*** + *N13O14N15* ***BEND(23)*** + *C8N7C12* ***BEND(13)*** + *O10C11C12N7* ***TORS(11)***
1120	1119	*O10C9* ***STRE(15)***+ *O10C11* ***STRE(18)*** + *O10C11C12N7* ***TORS(10)***+ *C9O10C11C12* –***TORS(12)*** + *C8C12C5N7* ***oop(10)***
1195	1193	*N7C8* ***STRE(21)***+ *N7C12* ***STRE(10)***+ *H19C1C6* ***BEND(15)***
1264	1251	*O17N16* ***STRE(10)***+ *O18N16* ***STRE(17)***+ *C4N15O14* ***BEND(14)***+ *H21C8C9* ***BEND(12)***+ *H24C9H23* ***BEND(22)***+ *H26C11H25* ***BEND(27)***+ *H22C8N7C12* ***oopt(11)***
1306	1303	*H21C8C9* ***BEND(14)***+ *H25C11O10* ***BEND(13)***+ *H22C8N7C12* ***oopt(10)***
1330	1326	*H23C9O10* ***BEND(33)*** + *H25C11O10* ***BEND(27)***
1356	1349	*O17N16* ***STRE(11)***+ *H27C12N7* ***BEND(10)*** + *C3N13O14* ***BEND(16)*** + *N13O14N15* ***BEND(12)*** + *H24C9O10C11* ***oopt (10)***
1406	1389	*N15C4* ***STRE(12)***+ *C4N15O14* ***BEND(10)*** + *C3N13O14* ***BEND(16)***+ *N13O14N15* ***BEND(12)*** + *H27C12N7C8* ***TORS(20)***
1470	1482	*N15C4* ***STRE(15)*** + *C6C1* ***STRE(16)*** + *C5C6* ***STRE(14)*** + *C2C3* ***STRE(20)*** + *H22C8H21* ***BEND(62)***
1510	1545	*O17N16* ***STRE(14)***+ *O18N16* ***STRE(15)***+ *H24C9H23* ***BEND(33)***+ *H26C11H25* ***BEND(38)***
1589	1597	*C1C2* ***STRE(12)*** + *C6C1* ***STRE(12)*** + *N7C5* ***STRE(11)*** + *H19C1C6* ***BEND(15)***
1646	1643	*N13C3* ***STRE(30)*** + *N15C4* ***STRE(20)*** + *C1C2* ***STRE(10)*** + *C5C6* ***STRE(11)*** + *C2C3* ***STRE(11)***
3017	2865	*C11H26* ***STRE(60)***+ *C9H23* ***STRE(31)***
3048	2992	*C8H22* ***STRE(92)***
3125	3125	*C9H24* ***STRE(76)***+ *C11H25* ***STRE(17)***
3169	3170	*C8H21* ***STRE(93)***
3227	3216	*C1H19* ***STRE(96)***

STRE: stretching; **BEND**: bending; **oop**: out of plane; **TORS**: torsion, ***oopt:*** out of plane torsion.

* *Most harmonic patterns are composed of various local modes. This table lists only the local modes that have the highest impact.*

Sundaraganesan and colleagues [70] have attributed the stretching frequencies of C–N and C═N band vibrations to 1302 cm^{-1} and 1689 cm^{-1}, respectively. Kahovec and team [71], on the other hand, have assigned the stretching frequency of C═N as 1617 cm^{-1}. Ultimately, all C–N and C═N infrared spectral ranges were computationally assessed. The DFT/B3LYP approach predicts the N–O stretching vibrations at 821 cm^{-1} (TED = 58%), 908, 1026, 1071, 1264, 1356, and 1510 cm^{-1}, and these frequencies are consistent with those experimentally detected.

4.4. NBD-morph adsorption to heavy metal cations (Co^{2+}, Pb^{2+}, Mg^{2+}, Ag^{+}, Cu^{2+}, Hg^{2+}, Ni^{2+}, and Zn^{2+})

4.4.1. Structural, adsorption energy, and selectivity

Recently, the theoretical study of adsorption phenomena has become mandatory to understand the mechanisms of interactions between a chemical compound and such guests. In addition, the chemical groups that form the donor-acceptor couple with the guests must be visualized. In this work, we evaluated the ability and capacity of NBD-Morph to adsorb heavy cations. The interpretations of the interaction mechanisms have been taken into account. The charge transfer and adsorption energy formed between the NBD-Morph molecule and the cations have been discussed. The stable structures of all possible complexation of the cations with the synthesized molecule are shown in Fig. 6. The adsorption energies of all the conformations are outlined in Table 6. We have complexed our system by adding such a cation to all the acceptor sites that contain electronegative atoms of the oxygen type. Therefore, in this case, we will

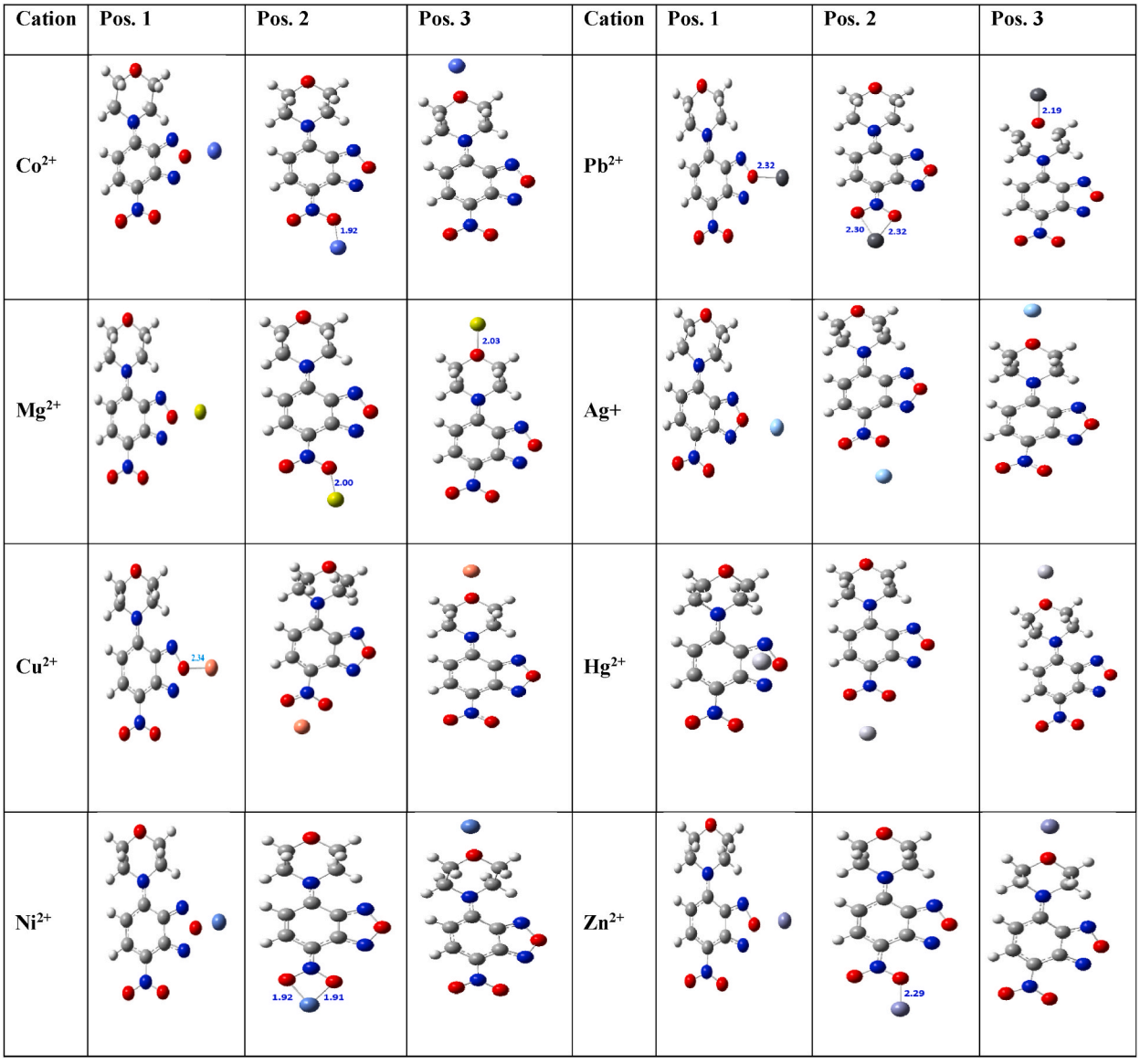

Fig. 6. The optimized structures of the NBD-Morph-X complexes (X = Co^{2+}, Pb^{2+}, Mg^{2+}, Ag^{+}, Cu^{2+}, Hg^{2+}, Ni^{2+}, and Zn^{2+}).

compare all the complexes to deduce the selective acceptor sites of the cations and to show the selectivity and sensitivity of NBD-Morph for these cations. In addition, we can mention which types of cations among the tested lists are more adsorbed by this molecule, which will be important in the near future when using this material in real applications. Concerning the NBD-Morph-Co2+ complexes, it is shown that the most stable complex is that of Pos.3. To achieve stabilization, d-electrons surrounding Co^{2+} engage in robust electrostatic interactions with the valence electrons of oxygen. NBD-Morph-Co2+/Pos.3 has an adsorption energy of approximately −67.47 kcal/mol. NBD-*M*-Pb2+/Pos.1 is found to be more stable than Pos.2 and 3. The Pb2+ cation is stabilized by an adsorption energy of −285.05 kcal/mol. Therefore, an evident electrostatic interaction forms between the oxygen atom, rich in electrons and linked to two nitrogen atoms, and the Pb2+ cation. This interaction may have a covalent nature, given the subsequent delocalization of electron density in the region between oxygen and the heavy metal Pb. From the adsorption energy values, it is indicated that the NBD-Morph molecule is very selective, more sensitive to Pb2+ than Co2+ cations. The contact between the Mg2+ and Ag + cations and the NBD-Morph compound has two adsorption energies in the order of −34.22 and −106.27 kcal/mol, respectively. It has been noted that NBD-Morph displays greater selectivity towards Ag^{+} as compared to the Mg^{2+} cation. Both metal cations are stabilized by electrostatic forces between d-electrons and the valence electrons of oxygen.

Consequently, charge transfer occurs between the two cations and two oxygen atoms. The NBD-Morph-Cu2+ and NBD-Morph-Hg2+ complexes are shown to be stabilized by two adsorption energies around −118.24 and −23.18 kcal/mol, respectively. It is concluded that the studied system is more selective and reactive to Cu2+ than Hg2+.

The more stable cation is stabilized by its interaction with the oxygen atoms located in front of it. As a result, d-electrons surrounding the Cu^{2+} cation directly interact with the valence electrons of the electronegative atom, forming a coupling donor-acceptor, Cu–O. It is apparent that nickel is more stable when it is located in a sandwich between two acceptor atoms (Pos.2). This atom is fixed by forming two electrostatic forces with two symmetrical oxygen atoms. Therefore, the d-electrons of the Ni cation serve as both a double donor and acceptor, leading to the formation of O–Ni–O interactions. The calculated Ead is determined to be −78.28 kcal/mol. In contrast, Zn2+ exhibits greater stability when captured near a single oxygen atom, as visualized in Fig. 7 (Pos.3). The NBD-Morph-Zn2+ complex is characterized by an adsorption energy in the range of −31.79 kcal/mol. NBD-Morph is found to be more selective toward the Ni2+ cation than the Zn2+ cation. According to the adsorption energy, charge transfer mechanism, selectivity, and reactivity properties, it is clear that the NBD-Morph molecule is suitable to adsorb heavy metals where the cation is located in front of the oxygen atoms of the heterocyclic, which contains one oxygen atom and one nitrogen atom (Pos. 3). It is also concluded that when this molecule adsorbs a cation on a sandwich between two oxygen atoms or when the cation exists in front of an oxygen and two nitrogen atoms, it has an average capacity to attack the cation.

If, in summary, the efficiency of NBD-Morph for adsorbing heavy cations is rearranged as follows: NBD-Morph-Pb2+ < NBD-Morph-Cu2+ < NBD-Morph-Ag+ < NBD-Morph-Ni2+ <NBD-Morph-Zn2+ <NBD-Morph-Hg2+. The mechanism of charge transfer and the formation of donor and acceptor, as well as the type of cation-binding interaction in such an active site, are well identified using MEP-3D and HS-2D fingerprint plots in the following paragraph.

4.4.2. QTAIM topological analyses

The use of QTAIM analysis [72–75] has been progressing consistently as a powerful method for displaying the qualities and categories of forces that develop during the interactions between electron donors and electron withdrawing groups. This method

Table 6
The computed adsorption energies of studied systems at the B3LYP-D3/LanL2DZ level of theory.

Complex/position	$E_{ad} + E_{BSSE}$ (a.u)	$E_{ad} + E_{BSSE}$ (eV)	$E_{ad} + E_{BSSE}$ (kcal/mol)
NBD-Morph-Co^{2+}/Pos.1-3	−0,087755283	−2,387935332	−55,06644008
	−0,104122073	−2,833296965	−65,33660081
	−0,10753498	−2,926166601	−67,47819995
NBD-Morph-Pb^{2+}/Pos.1-3	0,454272281	12,36133932	285,0558563
	0,402316956	10,94756738	252,4538899
	0,423258943	11,51742608	265,5949867
NBD-Morph-Mg^{2+}/Pos.1-3	−0,032014558	−0,871157742	−20,08913515
	−0,051801911	−1,409597341	−32,50569915
	−0,054539432	−1,484088846	−34,22349358
NBD-Morph-Ag^{+}/Pos.1-3	−0,161230467	−4,387290607	−101,172118
	−0,166722863	−4,536745842	−104,6185965
	−0,169362447	−4,608572354	−106,2749355
NBD-Morph-Cu^{2+}/Pos.1-3	−0.171207662	−4.658783053	−107.4328079
	−0,183354506	−4,989314469	−115,0549525
	−0,188444608	−5,127822762	−118,2489915
NBD-Morph-Hg^{2+}/Pos.1-3	−0,036955606	−1,005610082	−23,18964277
	−0,032949315	−0,896593695	−20,67569516
	−0,034235736	−0,931598883	−21,48292434
NBD-Morph-Ni^{2+}/Pos.1-3	−0,073970512	−2,012833793	−46,41649628
	−0,124762004	−3,394936319	−78,28815751
	−0,08846556	−2,407262893	−55,5121389
NBD-Morph-Zn^{2+}/Pos.1-3	−0,028569801	−0,777421426	−17,92755013
	−0,050415077	−1,371859785	−31,63546082
	−0,050675168	−1,378937199	−31,79866792

describes the bonding path between the two systems by mapping the critical points between the atoms that form the interaction. At each bond critical point (BCP), topological parameters can be determined, including the electron density (ρ(r)), the Laplacian of electron density ($\nabla^2\rho(r)$), the kinetic energy density (G(r)), the potential energy density (V(r)), and the interaction energy (E_{HB}). These parameters have been arranged in Table 7. QTAIM plots of the most stable complexes (NBD-Morph-Pb^{2+}/Pos.1, NBD-Morph--Cu^{2+}/Pos.2, NBD-Morph-Ag^{+}/Pos.3, and NBD-Morph-Ni^{2+}/Pos.2) are also visualized in Fig. 7. It is shown that the electron density of NBD-Morph-Pb^{2+} varies from 0.0141 a.u. to 0.0232 a.u. The Laplacian ranges from 0.0659 a.u. to 0.0920 a.u. A positive value of $\nabla^2\rho(r)$ indicates the formation of covalent bonds in these BCPs. In BCP 4, the $|V(r)|/G(r)$ ratio is found to be around 1.17542 a.u. This value is higher than the unit ($|V(r)|/G(r) > 1$). The covalent nature of the bond between the Pb^{2+} cation and the NBD-Morph compound is clarified based on the Bianchi et al. [76] rule. This finding is strongly supported by the significant interaction energy (E_{HB}) value of -45.82 kJ mol^{-1}.

As illustrated in Fig. 7, it can be observed that Pb^{2+} established a single covalent bond with the oxygen atom of NBD-Morph to maintain stability within every active region. The QTAIM results show that the NBD molecule is selective for the Pb^{2+} cation. In the case of NBD-Morph-Cu^{2+}, it is observed that the Cu^{2+} cation forms two coordination bonds with NBD-Morph to achieve stabilization. These two interactions are responsible for the efficiency of the capture of the NBD molecule by the Cu^{2+} cation. These bonds are established between a copper cation and two oxygen acceptor atoms of the NBD molecule. It shows a ρ(r) in the range of 0.0102–0.0750 a.u. The higher Laplacian values are observed in BCP 4, 5, which are equal to 0.4606 a.u. and 0.4586 a.u., respectively. The positive Laplacian values mean that these bonding interactions are covalent. The Cu^{2+} cation is stabilized by two coordination bonds with NBD-Morph, with bond energies in the order of -153.59 and -154.90 kJ mol^{-1}.

The $|V(r)|/G(r)$ ratio for BCP 4 and BCP 5 appears greater than or equal to unit. These findings indicate that the interaction is a covalent bond, hence the good selectivity of the NBD-Morph molecule to the Cu2+ cation. In comparison between the NBD-Morph-Pb2+ and the NBD-Morph-Cu2+, it is concluded that the NBD is more selective for the copper cation than plumb. From Fig. 7, it is obtained that Ni2+ is stabilized in its interaction with the NBD compound by the formation of two covalent interactions. These bindings are characterized by greater interaction energies of -197.30 (BCP4) and -195.07 (BCP5) kJ.mol-1, respectively. Furthermore, these findings are strongly supported by significant electron densities of 0.0890 atomic units and 0.0882 atomic units, respectively. In these BCPs, the Laplacian is obtained around 0.5000 a.u. The positive value of $\nabla^2\rho(r)$ justifies that the nickel is well stabilized by the covalent bond. As a result, the NBD molecule is highly selective for the Ni^{2+} cation. In another scenario, if other metals coexist in the same environment as nickel, NBD-Morph can potentially interact with various metals, thereby reducing the detection effectiveness of Ni^{2+}.

For the NBD-*M*-Ag^{+} complex, it is obtained that the Ag^{+} is stabilized by covalent interaction with the oxygen atom of the NBD-Morph. This interaction has a higher energy value of around -64.98 kJ.mol-1. In BCP4, it is found that $\rho(r) = 0.0378$ a.u. and $\nabla^2\rho(r) = 0.2018$ a.u. It is concluded from the higher electron density and the lower Laplacian at the level of BCP4 that this interaction is the strongest one. Therefore, the NBD-Morph is suitable to capture the Ag^{+} cation. In comparison to the results, we confirmed that NBD-Morph is more selective for Cu^{2+} and Ni^{2+} than Ag^{+} and Pb^{2+}. Finally, the topological QTAIM analysis indicates that the NBD-Morph my serve as an efficient probe for Ni^{2+}.

4.4.3. *MEP plots and Hirshfeld surface analyses*

The Hirshfeld surface (HS) and two-dimensional (2D) fingerprint diagrams are effective methods for understanding the intermolecular interactions between atoms [77–79]. Herein, we examined the d_{norm} utilizing the shape index to demonstrate that the cation is supported by powerful interactions. Furthermore, the MEPs mapping of the most stable complexes were produced to illustrate the

Table 7
The topological parameters (in a.u.): ρ(r), $\nabla^2\rho(r)$, (G(r), V(r), E_{int}, in kJ.mol^{-1} at selected BCPs.

Complexes	BCPs	ρ(r)	$\nabla^2\rho(r)$	G(r)	V(r)	$\lvert V(r)\rvert/G(r)$	E_{HB}
NBD-Morph-**Pb^{2+}**	**BCP1**	0.0150	0.0672	0.0146	−0.0112	0.78	−14.04
	BCP2	0.0232	0.092	0.0216	−0.0199	0.92	−26.12
	BCP3	0.0141	0.0659	0.0133	−0.0102	0.76	−13.42
	BCP4	0.0567	0.2347	0.0297	−0.0349	1.17542	−45.82
NBD-Morph-**Cu^{2+}**	**BCP1**	0.0149	0.0674	0.0137	−0.0107	0.78	−14.04
	BCP2	0.2030	0.0920	0.0214	−0.0198	0.92	−25.99
	BCP3	0.0102	0.0487	0.0095	−0.0068	0.71	−8.92
	BCP4	0.0749	0.4586	0.0116	−0.1175	1.00	−153.59
	BCP5	0.0750	0.4606	0.0116	−0.1181	1.01	−154.90
NBD-Morph-**Ni^{2+}**	**BCP1**	0.0151	0.0678	0.0169	−0.0108	0.63	−14.17
	BCP2	0.0232	0.0923	0.0215	−0.0200	0.93	−26.25
	BCP3	0.0099	0.0474	0.0092	−0.0066	0.71	−8.66
	BCP4	0.0890	0.5007	0.1377	−0.1503	1.09	−197.30
	BCP5	0.0882	0.4977	0.1365	−0.1486	1.08	−195.07
NBD-Morph-**Ag^{+}**	**BCP1**	0.0149	0.0676	0.0138	0.0030	0.77	−14.04
	BCP2	0.0234	0.0932	0.0218	0.14	0.93	−26.64
	BCP3	0.0123	0.0580	0.0116	0.0029	0.75	−11.42
	BCP4	0.0378	0.2018	0.0500	0.0004	0.99	−64.98

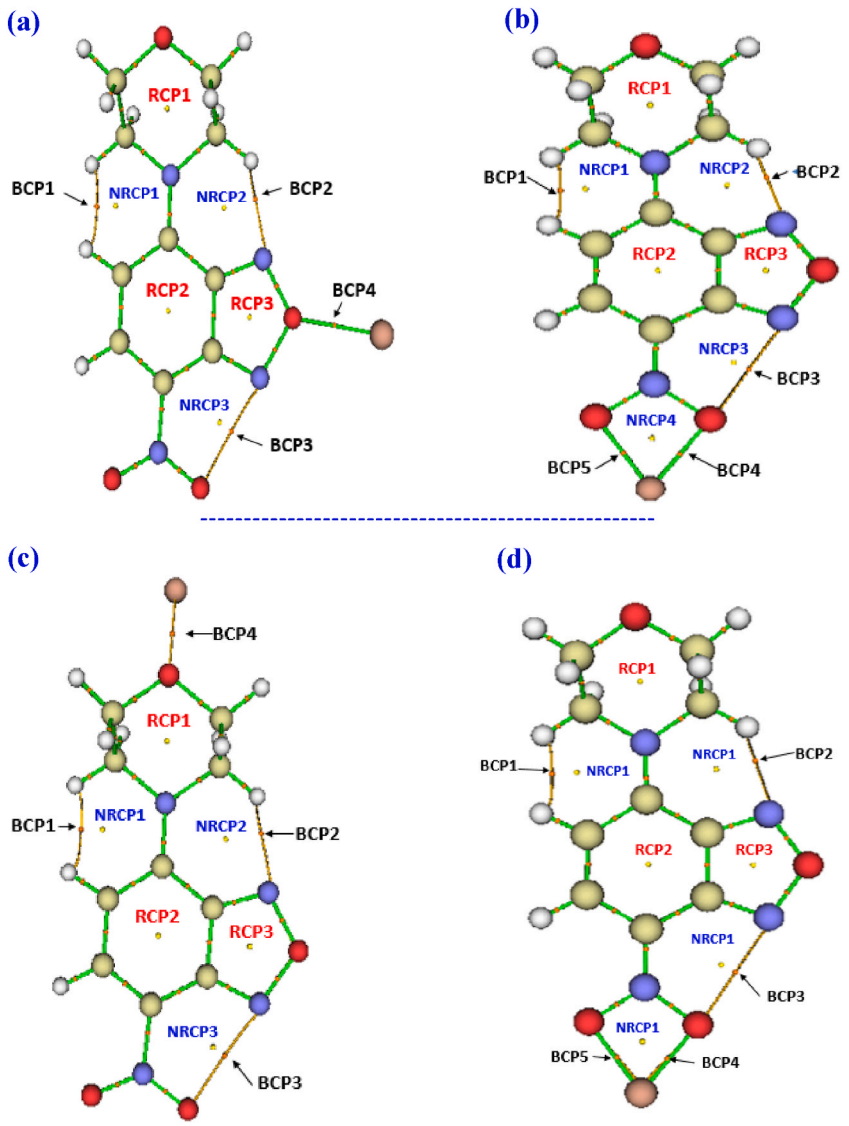

Fig. 7. QTAIM graphs of the NBD-Morph-Pb^{2+} (a), NBD-Morph-Cu^{2+} (b), NBD-Morph-Ag^{+} (c), and NBD-Morph-Ni^{2+} (d) complexes.

impact of the existence of metallic cations on the electrophilic or nucleophilic index of the NBD-Morph compound [80]. Moreover, looking at MEP surfaces is very useful to recognize the sites of electron acceptor and electron donor populations in the presence of metal cations. MEP, HS, and the 2D fingerprint plots encompassing interactions (100% total) within the studied compound and the Cu2+, Ni2+, Ag+, and Pb2+ cations are shown in Figs. 8–10, respectively.

From MEP plots (see Fig. 8), it is obtained that there are negative electron concentrations at the NBD surface levels and positive electron concentrations surrounding Cu and Ni cations. This result deduces that there is a donor-acceptor couple between the compound and the guest. From the MEP plots, it is deduced that the O–Cu–O group appears positively charged. This idea may be explained by the fact that the lone pair electrons of the oxygen atoms are torn off by the nearby N and H atoms, while the electrons given up by the cations are placed in the empty orbitals surrounding the oxygen atoms; hence, the appearance of electrophile sites surrounds the O–Cu/Ni–O groups. Concerning the NBD-Morph-Ag^{+} complex, it is noted that dark red spots surround the group O–N–O, while the entourage of the other groups appears pale red. It is shown that the binding site between Ag and NBD-Morph is practically non-colored, explaining that all the valence electrons are taken and the others are attracted by the other part of NBD-Morph containing excess oxygen acceptor electrons. Furthermore, in the NBD-Morph-Pb^{2+} complex, there are light red spots surrounding the O–N–O group and a light blue spot surrounding the cation. This observation indicates that, despite the fact that the electrons given up by the metal cation still react with the oxygen to form a covalent bond; the valence electrons of the N atoms are absorbed by the Pb^{2+} cation.

To understand the nature of bindings and the group that promotes the interactions between Cu2+, Ni2+, Ag+, and Pb2+ cations and the NBD-Morph compound, we studied the Hirshfeld surface analysis parameters: d_{norm}, shape index, and curvedness, as depicted

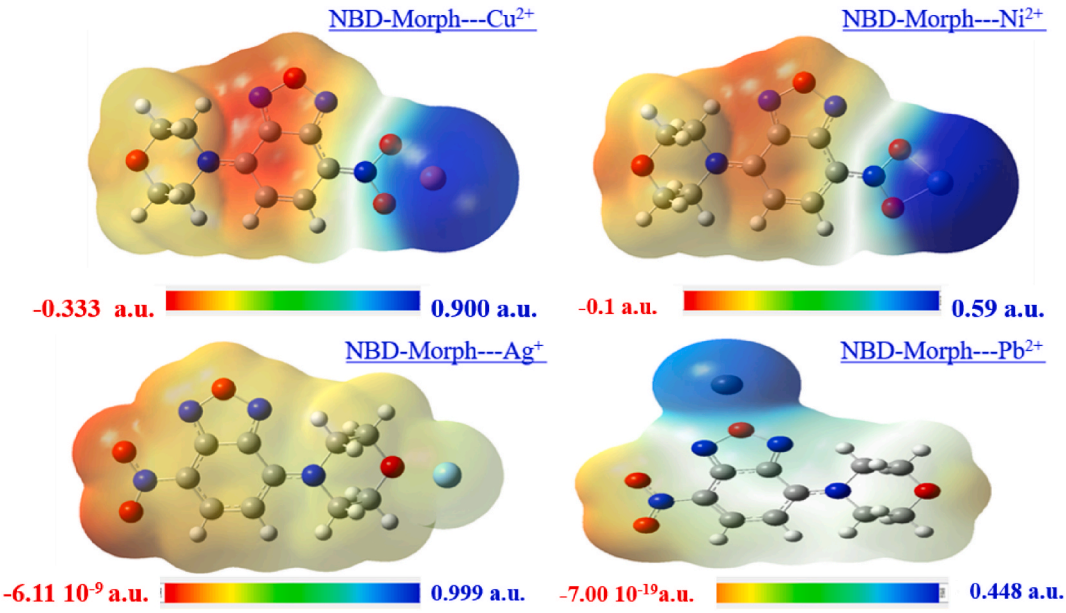

Fig. 8. MEP plots of the investigated stable complexes. The red color denotes negative potential sites, while blue represents positive ones. A yellow-green color is used to indicate neutral potential sites.

in Fig. 9 (a, b, c, and d). The d_{norm} values of NBD-Morph-Cu^{2+} ranged from −1.237 (red) to 3.594 Å (blue); for NBD-*M*-Ni^{2+}, the d_{norm} values ranged from −1.239 Å to 5.156 Å, while the d_{norm} value for NBD-*M*-Ag^{+} varies from −1.237 to 5.356 Å, and the HS analysis of NBD-Morph-Pb^{2+} showed d_{norm} values between −1.239 Å and 5.692 Å. The shape index values for all the complexes are varied between 1 (concave) and −1 (convex). The curvedness varies, ranging from −4 to 0.4 Å. As shown in Fig. 9, the curvedness surfaces of all complexes clearly indicate that green or yellowish green colors surround the active site for the studied complexes, justifying the fixing of the cations in their sites by covalent interactions. Moreover, in Fig. 10, we present a comprehensive representation of the 2D fingerprint plots, which capture the most important interactions observed between cations and the NBD-Morph compound under investigation. Additionally, we depict the percentage distribution of contact contributions for each complex using a pie chart.

Starting with Cu2+ shows that a red spot can be seen between the metal cation and the two oxygen atoms. This concept verifies the QTAIM investigations showing that the Cu^{2+} ion is stabilized by two covalent interactions. Based on the 2D fingerprint diagrams, it is inferred that the dominant bonding interactions involve Cu···O and Cu···H, which account for 79.4 % and 13.10 % of the total system packing, respectively. The atoms N and C do not intervene in the binding site, which is characterized by minor interactions involving Cu···N and Cu···C comprising almost 3.7 % and 2.3 % of all interactions, respectively. The sharp peak appearing in Fig. 2D-fingerprint plot is a good sign that the cation is fixed by covalent interactions. It has been determined that the NBD-Morph compound is appropriate for capturing the Cu^{2+} ion. Concerning the NBD-Morph-Ni^{2+} complex, it is also evident in the d_{norm} and shape index; the appearance of the red spots deduces that there is a formation of the double donor-acceptor between the Ni and the two close neighboring oxygen atoms. The fingerprint plot shows that the Ni···H, and Ni···O contacts comprise 16.40 % and 76.40 % of the total Hirshfeld surface area, respectively. Ni···C/C···N contacts make the least contribution to the total Hirshfeld surface area, with 3.10 % and 2.80 %, respectively. Therefore, the major interaction is Ni···O, and it promotes binding for cation stability in each active region. It is deduced that the NBD-Morph is very suitable for Ni^{2+} sensors. About the Ag^{+} cation, from the d_{norm} Figures, it is noted that there are large red spots between the cations and their close neighboring atoms, but it appears that the Ag···O interaction is predominant, with a contribution of approximately 74.60 %. Ag···H/H···Ag is the second most significant contribution in the NBD-Morph-Ag^{+}, with a percentage of 16.50 %. The other atoms have minor interactions. The sharp peak obtained from the 2D fingerprint plot confirms the QTAIM study that the Ag^{+} cation is bound by a covalent interaction. Ultimately, it has been determined that NBD-Morph exhibits high selectivity towards the Ag^{+} ion. Finally, the HS/2D fingerprint plot indicates that Pb^{2+} is well stabilized through coordination bonding with the NBD-Morph compound, as evident from the d_{norm} and shape index. It is concluded from HS/2D-fingerprint plots that Ni^{2+} forms the strongest interaction with O atoms in each active region, indicating the stronger stability of the O···Ni···O interactions than other bindings.

A correlation between MEP and HS/2D fingerprint plots indicates that the NBD-Morph-X (X = Cu^{2+}, Ni^{2+}, Ag^{+}, or Pb^{2+}) complexes are very efficient to use as a sensitive layer in sensor design.

4.4.4. ELF-LOL topography

The electron localization function (ELF) is an efficient theory to show the electron occupation sites after sensing cations [81–83]. It is indicated that a donor-acceptor couple exists between selected cations and the NBD-Morph molecule. As a result, the NBD-Morph's sensitivity to Cu^{2+}, Ni^{2+}, Ag^{+}, and Pb^{2+} cations has been confirmed. The ELF theory is elaborated by Becke and Edgecombe [84].

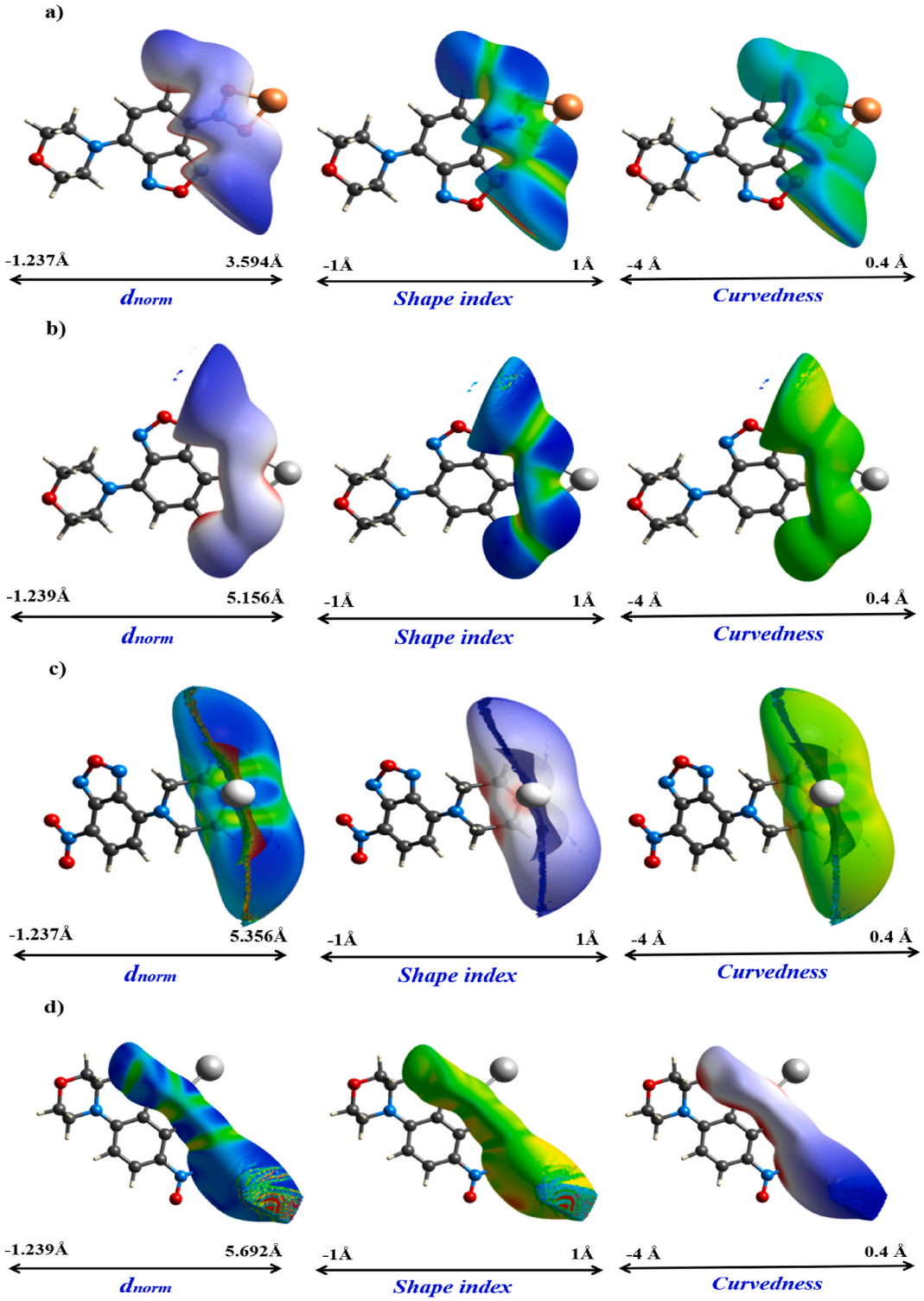

Fig.9. Hirshfeld surfaces mapped with dnorm, shape index, and curvedness of NBD-Morph-Cu^{2+} (a), NBD-Morph-Ni^{2+} (b), NBD-Morph-Ag^{+} (c), and NBD-Morph-Pb^{2+}(c).

Domingo has utilized this theory to demonstrate the most reactive compound among the three atomic components (TACs) and their reactivity's in [3 + 2] cycloaddition reactions [85]. In addition, we have studied the LOL topography to show the localization of the lone pair electron in the binding interaction regions [86,87]. Accordingly, we can verify the presence of coordinate covalent

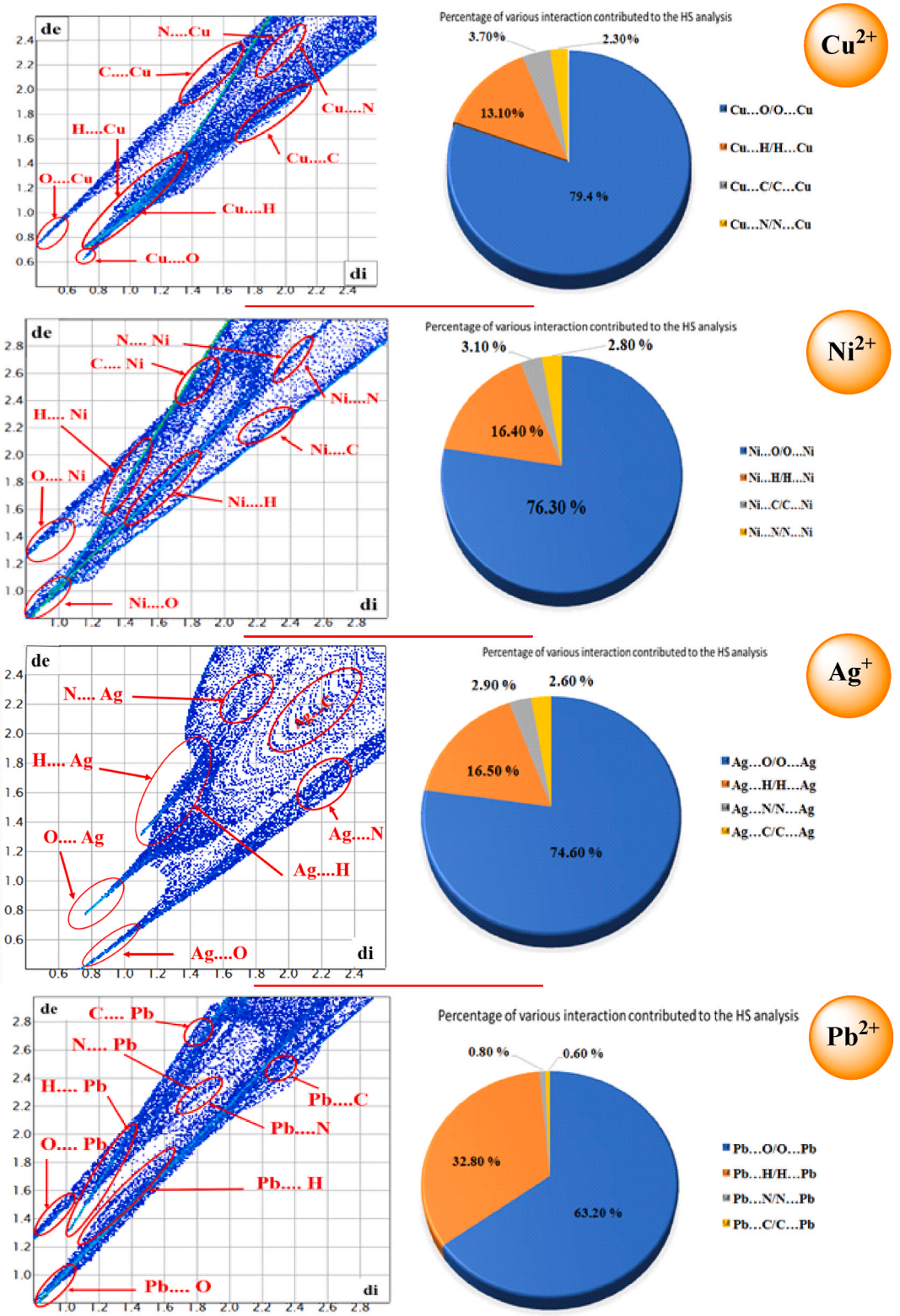

Fig. 10. 2D fingerprint plots and relative contributions of various intermolecular interactions to the Hirshfeld surface areas in NBD-Morph-Cu^{2+}, NBD-Morph-Ag^{+}, NBD-Morph-Pb^{2+}, and NBD-Morph-Ni^{2+} of the bonding interactions between cations and the NBD-Morph molecule.

interactions between cations and NBD-Morph. Herein, we have investigated the ELF and LOL theories based on the localization of the BCPs in all active regions. The 2D-ELF maps are computed. The 2D-ELF and 3D-LOL plots are depicted in Fig. 11. In the NBD-Morph-Cu^{2+} complex, as revealed by 2D-ELF, it is evident that the red patch around the atoms involved in coordination with the metal ions is significantly reduced. Additionally, 3D-LOL illustrates several large pink spots around the two-acceptor oxygen atoms, suggesting the presence of excess non-binding electrons responsible for covalent interactions with the Cu^{2+} cation. A non-bonded pair in the valence shells of two oxygen atoms can undergo a covalent interaction with the Cu^{2+}cation.

This finding corroborates our QTAIM results, indicating that copper cations are stabilized through coordination bonding with NBD-Morph in each active region. The ELF value varies from 0.8 to 1 a.u. It is inferred that NBD-Morph exhibits high selectivity for the Cu^{2+} cation. In Fig. 11, a faint red spot surrounding a blue color indicates a delocalization of electron density, leading to the fixation of this ion through a coordination-covalent interaction with the oxygen atoms in front. The 3D-LOL plots, revealing numerous scattered pink spots away from the interaction area, support this finding. This observation suggests that the non-binding lone pairs are strengthened by the electrostatic forces exerted by the d-electrons around the cation, particularly away from the region of interactions. This outcome can be elucidated by the instability of the interaction between O–Ni–O in comparison to O–Cu–O. The ELF value is around 0.8 a.u. NBD-Morph exhibits selective reactivity to the Ni^{2+} cation. Moreover, it is noteworthy that the interaction environment between the Ag^{+} cation and the oxygen acceptor atom is characterized by a reduced quantity of unshared pairs in the oxygen valence shell, as illustrated by the LOL plots. This observation is further confirmed by the absence of the large pink spot between Ag^{+} and O. Additionally, the LOL plots in the figure suggest an unstable interaction between Ag and O. Furthermore, in the 2D-ELF analysis, a blue circle around the Ag^{+} cation reveals the presence of a delocalized electron cloud around it.

The ELF value appears on the active site, varying from 0.6 a.u. to 0.75 a.u. From Fig. 3D-LOL, the Pb–O bond appeared stable compared to the Ag–O bond. In Fig. 11, concerning NBD-Morph-Pb^{2+}, regions with high ELF (1 a.u.) are observed around the Pb ion, indicating the presence of highly localized bonding and non-bonding electrons in this area. This facilitates the formation of a coordinate covalent bond with our material. NBD-Morph is able to capture the Pb^{2+} cation, but the Pb–O interaction is less stable than that of the O–Cu–O and O–Ag–O bindings.

The 2D-ELF and 3D-LOL plots have shown and confirmed that the NBD-Morph-X (Cu2+, Ni2+, Ag+, and Pb2+) complex is very powerful for use in the manufacture of a high-performance chemical sensor.

4.4.5. *Chemical sensor response for Ni^{2+} cation*

4.4.5.1. Impedimetric detection. The electrochemical response of NBD-Morph/Pt towards nickel was investigated using electrochemical impedance spectroscopy (EIS). Fig. 12-a illustrates the Nyquist plot of the ligand/Ni^{2+} complex upon addition of Ni^{2+} ions (from 10^{-6} to 10^{-3} M). It has been stated that the diameter of impedance spectra of the NBD-Morph-modified electrode significantly reduced upon varying Ni^{2+} concentrations. A clear change was evidently observed when the nickel detection membrane interacted with NBD-Morph, particularly at lower frequencies where the most significant variation was detected. To determine the performance of our electrochemical sensor, we plotted the calibration curve, as shown in Fig. 12-b.

This figure depicts the change in log (Z_0/Z) at a frequency value equal to 1 Hz as a function of the logarithm of nickel concentration, where Z_0 and Z present the impedance values before and after the injection of nickel, respectively. The sensor was found to respond linearly to nickel concentrations ranging from 10^{-10} M to 10^{-5} M in accordance with the following equation: log (Z_0/Z) = 0.04 × log (Ni^{2+}) + 0.26, with a correlation coefficient of R^2 = 0.97, where the slope is −0.01 of the sensor sensitivity. The sensor's limit of detection (LOD) was approximated to be $8.63.10^{-7}$ using the equation LOD = (3 standard deviations)/slope. Thus, the NBD-Morph compound is recommended as a sensor element, demonstrating its potential strength in the design of chemical sensors.

4.4.5.2. Selectivity study. We explored potential interferences in the quantitative measurement of nickel on a platinum electrode modified with NBD-Morph by introducing interfering ions at concentrations 100-fold higher than that of Ni^{2+} ions. Various interfering ions, including Co^{2+}, Pb^{2+}, Mg^{2+}, Ag^{+}, Cu^{2+}, Hg^{2+}, and Zn^{2+}, were subjected to testing (see Table 8 and Fig. 13).

The results revealed that the impedance signal of Ni^{2+} exhibited a variation of less than 6% in the presence of these interferents. Consequently, the proposed sensor demonstrates good selectivity for accurately determining Ni^{2+}.

4.4.5.3. Equivalent circuit modeling in EIS. The Nyquist spectra exhibit a distinct semicircle with a broad diameter, indicating the overlap of two semicircles. The equivalent circuit depicted in Fig. 14 can effectively model the experimental data.

This circuit consists of two components arranged in series with the electrolyte resistance (Rs). The first component, observed at higher frequencies and characterizing the electrochemical phenomena at the electrolyte/film interface, includes a film resistance (R_m) and a film capacitance (CPE_f). The second component, at low frequencies, comprises (R_{ct}, CPE_{dl}) and describes the electrochemical phenomena occurring at the Pt/aqueous solution interface. In this context, R_{ct} represents the charge transfer resistance, and CPE_{dl} represents double-layer capacitance.

The impedance of a Constant Phase Element (CPE) in an electrical circuit can be expressed using the following equation: $Z_{CPE} = \frac{1}{Q(jw)^n}$. where Q (F) is a frequency-independent factor that provides information about homogeneity, roughness, and surface porosity, j is the imaginary number, ω (rad.s^{-1}) is the angular frequency, and n is a correction factor ($0 < n < 1$). The values derived from the fitting model are summarized in Table 9.

The solution resistance (Rs) remains nearly consistently stable across all concentrations of nickel. Both the values of CPE_f and CPE_{dl} are unaffected by the increasing nickel concentration, while both the film resistance (R_f) and the charge transfer resistance (R_{ct}) exhibit

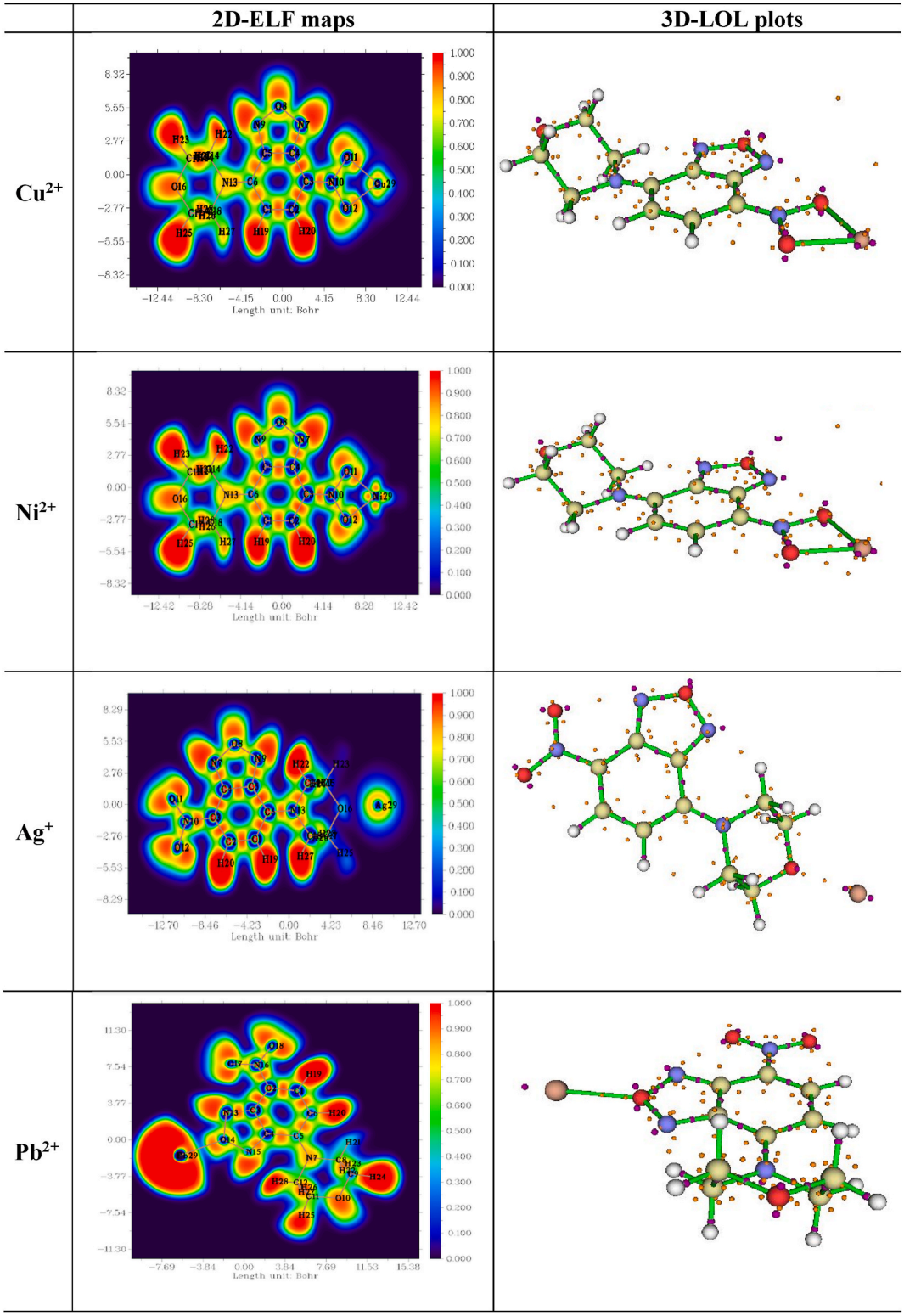

Fig. 11. 2D-ELF and 3D-LOL plots of the most stable complexes.

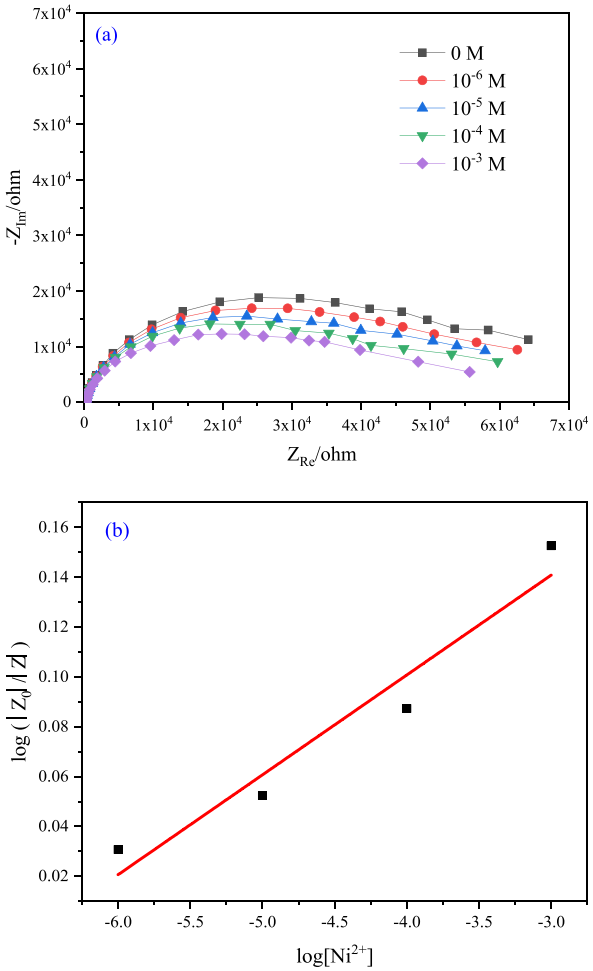

Fig. 12. Nyquist plot (a) and the variation of log (Z_0/Z) (b) of the structures after the addition of Ni^{2+} ions.

Table 8
Influence of interfering ions on the impedance response to 10^{-5} M Ni^{2+} in ammonium acetate buffer at pH 7.

Interferents	Impedance change
Co^{2+}	3.1 %
Pb^{2+}	5.1 %
Mg^{2+}	3.7 %
Cu^{2+}	5.2 %
Hg^{2+}	3.4 %
Zn^{2+}	5.5 %
Ag^{+}	2.8 %

a noteworthy decrease with the rising nickel concentration. On the one hand, the film resistance decreases as the nickel concentration increases. This trend could be attributed to an improvement in the ionic conductivity of the NBD-Morph film. Moreover, the charge transfer resistance diminishes with the addition of nickel, indicating an enhanced electron transfer to the Pt/electrolyte interface with the introduction of nickel ions into the electrolyte solution.

5. Conclusion

In this paper, the complexation behavior of the NBD-Morph ligand towards metal cations (Co^{2+}, Pb^{2+}, Mg^{2+}, Ag^{+}, Cu^{2+}, Hg^{2+}, Ni^{2+}, and Zn^{2+}) has been investigated. The NBD-Morph ligand structure was confirmed through FT-IR and ^{1}H NMR spectroscopic analyses. Theoretical predictions, based on the DFT/B3LYP method, were validated by comparing calculated IR and ^{1}H NMR spectra

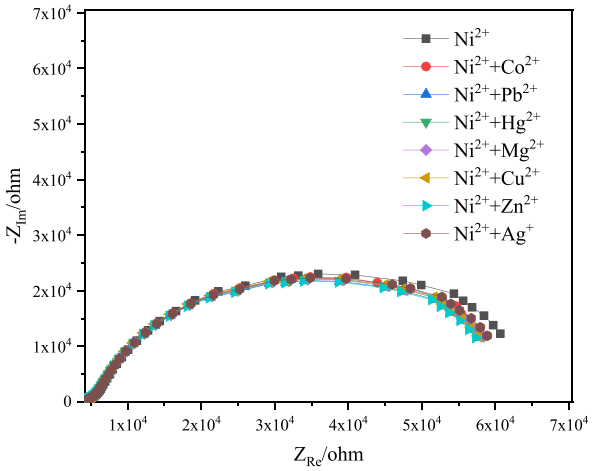

Fig. 13. Impedance spectra of Ni^{2+} solution in the absence and presence of interfering ions.

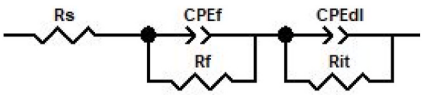

Fig. 14. Equivalent circuit used for impedance modeling.

Table 9
Fitting data of the NBD-Morph/Pt for different nickel concentrations.

$[Ni^{2+}]$ (M)	R_s (Ω)	CPE_f(μF)	n_1	R_f (Ω)	CPE_{dl}(μF)	n_2	R_{it}(Ω)	χ2 (10^{-4})
0	185.5 ± 1.01	14.76 ± 1.01	0.84	33093 ± 950	1.70 ± 0.21	0.89	33138 ± 907	3
10^{-6}	188.1 ± 1.2	15.04 ± 1.28	0.84	31818 ± 1024	1.80 ± 0.02	0.89	30035 ± 968	4.1
10^{-5}	187.4 ± 1.1	13.3 ± 1.12	0.85	29123 ± 926	1.78 ± 0.02	0.89	26665 ± 901	3.7
10^{-4}	187.7 ± 2.0	14.35 ± 1.69	0.85	28741 ± 1097	1.76 ± 0.03	0.89	25255 ± 1195	9.3
10^{-3}	189.6 ± 2.2	15.3 ± 1.52	0.85	28557 ± 0.141	1.84 ± 0.03	0.89	20538 ± 911	10.1

with experimental data. QTAIM-DFT topological analyses reveal that NBD-Morph forms coordinate covalent interactions with cations for stabilization. MEP, 2D-, and 3D-HS suggest a charge transfer between cations and the O—NBD-Morph compound, facilitating the uptake of selected cations. ELF and LOL topological analyses indicate the formation of a donor-acceptor couple upon addition of Ni^{2+} or Cu^{2+} metal cations, underscoring the high selectivity of NBD-Morph for these cations. To support the findings, electrochemical measurements were conducted. The combined results confirm the complexation ability of the modified nitrobenzofurazan ligand with metal cations. Notably, NBD-Morph is found to be selective for Ni^{2+} cation, making the NBD-Morph-Ni^{2+} complex highly suitable as a sensitive membrane in the design of a chemical sensor.

Data availability

Data will be made available on request.

CRediT authorship contribution statement

Imen Chérif: Writing – original draft, Validation, Supervision, Software, Methodology, Conceptualization. **Bouzid Gassoumi:** Writing – original draft, Validation, Supervision, Software, Methodology, Conceptualization. **Hajer Ayachi:** Methodology, Conceptualization. **Mosaab Echabaane:** Writing – original draft, Software, Methodology, Formal analysis. **Maria Teresa Caccamo:** Validation, Supervision, Investigation. **Salvatore Magazù:** Validation, Supervision, Investigation. **Ayoub Haj Said:** Validation, Supervision. **Boubaker Taoufik:** Validation, Supervision, Investigation. **Sahbi Ayachi:** Writing – review & editing, Validation, Supervision, Software, Methodology, Investigation.

Declaration of competing interest

The authors declare that they have no known competing financial interests or personal relationships that could have appeared to

influence the work reported in this paper.

Acknowledgements

This work was realized in the frame of the Program ERASMUS + KA107, FSE 2014/2020 P.O.R. Sicilia Project no. 2020-1-IT02-KA107-078488, CUP J49J21003660006.

References

[1] J. Sun, M. Li, Z. Zhang, J. Guo, Unravelling the adsorption disparity mechanism of heavy-metal ions on the biomass-derived hierarchically porous carbon, Appl. Surf. Sci. 471 (2019) 615–620, https://doi.org/10.1016/j.apsusc.2018.12.050.
[2] M. Zhang, Y.Q. Liu, B.C. Ye, Colorimetric assay for parallel detection of Cd^{2+}, Ni^{2+} and Co^{2+} using peptide-modified gold nanoparticles, Analyst 137 (2012) 601–607, https://doi.org/10.1039/C1AN15909G.
[3] H. Zeng, L. Wang, D. Zhang, P. Yan, J. Nie, V.K. Sharma, C. Wang, Highly efficient and selective removal of mercury ions using hyperbranched polyethylenimine functionalized carboxymethyl chitosan composite adsorbent, Chem. Eng. J. 358 (2019) 253–263, https://doi.org/10.1016/j.cej.2018.10.001.
[4] M. Cegłowski, G. Schroeder, Removal of heavy metal ions with the use of chelating polymers obtained by grafting pyridine-pyrazole ligands onto polymethylhydrosiloxane, Chem. Eng. J. 259 (2015) 885–893, https://doi.org/10.1016/j.cej.2014.08.058.
[5] W.L. Chu, N.L. Dang, Y.Y. Kok, K.S.I. Yap, S.M. Phang, P. Convey, Heavy metal pollution in Antarctica and its potential impacts on algae, Pol. Sci. 20 (2019) 75–83, https://doi.org/10.1016/j.polar.2018.10.004.
[6] T.M. Zewail, N.S. Yousef, Kinetic study of heavy metal ions removal by ion exchange in batch conical air spouted bed, Alex. Eng. J. 54 (2015) 83–90, https://doi.org/10.1016/j.aej.2014.11.008.
[7] E.L. Cochrane, S. Lu, S.W. Gibb, I. Villaescusa, A comparison of low-cost biosorbents and commercial sorbents for the removal of copper from aqueous media, J. Hazard Mater. 137 (2006) 198–206, https://doi.org/10.1016/j.jhazmat.2006.01.054.
[8] Z. Gao, W. Zhan, Y. Wang, Y. Guo, L. Wang, Ya Guo, G. Lu, Aldehyde-functionalized mesostructured cellular foams prepared by copolymerization method for immobilization of penicillin G acylase, Microporous Mesoporous Mater. 202 (2015) 90–96, https://doi.org/10.1016/j.micromeso.2014.09.053.
[9] A.B. Dekhil, Y. Hannachi, A. Ghorbel, T. Boubaker, Comparative study of the removal of cadmium from aqueous solution by using low-cost adsorbents, Journal of Environmental Science and Technology 4 (2011) 520–533, https://doi.org/10.3923/jest.2011.520.533.
[10] A.B. Dekhil, Y. Hannachi, A. Ghorbel, T. Boubaker, Removal of lead and cadmium ions from aqueous solutions using the macroalga Caulerpa racemosa, Chem. Ecol. 27 (2011) 221–234, https://doi.org/10.1080/02757540.2010.529077.
[11] F. Qian, C. Zhang, Y. Zhang, W. He, X. Gao, P. Hu, Z. Guo, Visible light excitable Zn^{2+} fluorescent sensor derived from an intramolecular charge transfer fluorophore and its in vitro and in vivo application, J. Am. Chem. Soc. 131 (2009) 1460–1468, https://doi.org/10.1021/ja806489y.
[12] T. Yamaguchi, M. Asanuma, S. Nakanishi, Y. Saito, M. Okazaki, K. Dodo, M. Sodeoka, Turn-ON fluorescent affinity labeling using a small bifunctional *O*-nitrobenzoxadiazole unit, Chem. Sci. 5 (2014) 1021–1029, https://doi.org/10.1039/C3SC52704B.
[13] P.B. Ghosh, M.W. Whitehouse, 7-chloro-4-nitrobenzo-2-oxa-1,3-diazole: a new fluorigenic reagent for amino acids and other amines, J. Biochem. 108 (1968) 155–156, https://doi.org/10.1042/bj1080155.
[14] P.B. Ghosh, M.W. Whitehouse, Potential antileukemic and immunosuppressive drugs. Preparation and in vitro pharmacological activity of some 2,1,3-benzoxadiazoles (benzofurazans) and their N-oxides (benzofuroxans), J. Med. Chem. 11 (1968) 305–311, https://doi.org/10.1021/jm00308a027.
[15] D. Castagnolo, M. Pagano, M. Bernardini, M. Botta, Studies on the acylation of 4-(2-aminoethylthio)-7-nitrobenzofurazan: the role of bases in promoting the formation of fluorescent *S*-acyl derivatives through S-N Smiles rearrangement, Tetrahedron Lett. 53 (2012) 5008–5011, https://doi.org/10.1016/j.tetlet.2012.07.033.
[16] C. Toriumi, K. Imai, Determination of insulin in a single islet of langerhans by high-performance liquid chromatography with fluorescence detection, Anal. Chem. 74 (2002) 2321–2327, https://doi.org/10.1021/ac020043t.
[17] T. Kajiro, Y. Nakajima, T. Fukushima, K. Imai, A method to evaluate the renin-angiotensin system in rat renal cortex using a microdialysis technique combined with HPLC-fluorescence detection, Anal. Chem. 74 (2002) 4519–4525, https://doi.org/10.1021/ac020059j.
[18] (a) P.G. Farrell, F. Terrier, H.-Q. Xie, T. Boubaker, Reversal of the order of catalytic efficiency of primary and secondary amines in the ionization of a sterically hindered carbon acid, J. Org. Chem. 55 (1990) 2546–2548, https://doi.org/10.1021/jo00295a058;
(b) N.E. Guesmi, T. Boubaker, R. Goumont, Activation of the aromatic system by the SO_2CF_3 group: kinetics study and structure-reactivity relationships, Int. J. Chem. Kinet. 42 (2010) 203–210, https://doi.org/10.1002/kin.20446.
[19] (a) H. Raissi, H. Ayachi, F. Mahdhaoui, S. Ayachi, T. Boubaker, Relationships between experimental and theoretical scales of electrophilicity of 7-L-4-nitrobenzofurazans, J. Mol. Struct. 1224 (2021) 128843, https://doi.org/10.1016/j.molstruc.2020.128843;
(b) H. Raissi, I. Chérif, I. Aribi, H. Ayachi, A. Haj Said, S. Ayachi, T. Boubaker, Structure-property relationships in para-substituted nitrobenzofurazans: electrochemical, optical, and theoretical analysis, Chem. Pap. (2022), https://doi.org/10.1007/s11696-022-02150-y.
[20] H. Raissi, I. Chérif, H. Ayachi, A.H. Said, F. Hassen, S. Ayachi, T. Boubaker, Structure-Property relationships in benzofurazan derivatives: a combined experimental and DFT/TD-DFT investigation, in: Density Functional Theory - Recent Advances, New Perspectives and Applications, IntechOpen, 2021, https://doi.org/10.5772/intechopen.99246.
[21] H.C. Ting, Y.T. Yang, C.H. Chen, J.H. Lee, J.H. Chang, C.I. Wu, T.L. Chiu, C.F. Lin, C.L. Chung, K.T. Wong, Easy access to NO2 -containing donor-acceptor-acceptor electron donors for high efficiency small-molecule organic solar cells, ChemSusChem 9 (2016) 1433–1441, https://doi.org/10.1002/cssc.201600361.
[22] J. Hu, C. Li, Y. Cui, S. Liu, Highly selective colorimetric and fluorometric probes for fluoride ions based on nitrobenzofurazan-containing polymers, Macromol. Rapid Commun. 32 (2011) 610–615, https://doi.org/10.1002/marc.201100024.
[23] M.R. Crampton, R.E.A. Lunn, D. Lucas, σ-Adduct formation and oxidative substitution in the reactions of 4-nitrobenzofurazan and some derivatives with hydroxide ions in water, Org. Biomol. Chem. 1 (2003) 3438–3443, https://doi.org/10.1039/B307648M.
[24] B. Bernardim, P.M.S.D. Cal, M.J. Matos, B.L. Oliveira, N.M. Sáez, I.S. Albuquerque, E. Perkins, F. Corzana, A.C.B. Burtoloso, G.J. Osés, G.J.L. Bernardes, Stoichiometric and irreversible cysteine-selective protein modification using carbonylacrylic reagents, Nat. Commun. 7 (2016) 13128, https://doi.org/10.1038/ncomms13128.
[25] S. Kaviani, D.A. Tayurskii, O.V. Nedopekin, I. Piyanzina, DFT insight into Cd2+, Hg2+, Pb2+, Sn2+, As3+, Sb3+, and Cr3+ heavy metal ions adsorption onto surface of bowl-like B30 nanosheet, J. Mol. Liq. 365 (2022) 120131, https://doi.org/10.1016/j.molliq.2022.120131.
[26] S. Kaviani, M. Izadyar, M. Khavani, M.R. Housaindokht, A combined molecular dynamics and quantum mechanics study on the interaction of Fe3+ and human serum albumin relevant to iron overload disease, J. Mol. Liq. 317 (2020) 113933, https://doi.org/10.1016/j.molliq.2020.113933.
[27] S. Kaviani, S. Shahab, M. Sheikhi, M. Khaleghian, S. Al Saud, Characterization of the binding affinity between some anti-Parkinson agents and Mn2+, Fe3+ and Zn2+ metal ions: a DFT insight, Inorg. Chem. Commun. 128 (2021) 108582, https://doi.org/10.1016/j.inoche.2021.108582.
[28] S. Kaviani, S. Shahab, M. Sheikhi, M. Ahmadianarog, DFT study on the selective complexation of meso-2,3-dimercaptosuccinic acid with toxic metal ions (Cd2+, Hg2+ and Pb2+) for pharmaceutical and biological applications, J. Mol. Struct. 1176 (2019) 901–907, https://doi.org/10.1016/j.molstruc.2018.09.027.
[29] S. Kaviani, M. Izadyar, M.R. Housaindokht, A DFT study on the complex formation between desferrithiocin and metal ions (Mg2+, Al3+, Ca2+, Mn2+, Fe3+, Co2+, Ni2+, Cu2+, Zn2+), Comput. Biol. Chem. 67 (2017) 114–121, https://doi.org/10.1016/j.compbiolchem.2016.12.012.
[30] S. Kaviani, M. Izadyar, M.R. Housaindokht, A DFT study on the metal ion selectivity of deferiprone complexes, Comput. Biol. Chem. 86 (2020) 107267, https://doi.org/10.1016/j.compbiolchem.2020.107267.

[31] S. Kaviani, M. Izadyar, The possibility of iron chelation therapy in the presence of different HPOs; a molecular approach to the non-covalent interactions and binding energies, J. Mol. Struct. 1166 (2018) 448–455, https://doi.org/10.1016/j.molstruc.2018.04.065.

[32] E. Buncel, N.C. Offermanns, B.K. Hunter, A.R. Norris, σ-Complexes as biophysical and biochemical probes. Part II. Transformations of σ-complex intermediates from reaction of 4-nitrobenzofuroxan and methoxide ion, Can. J. Chem. 55 (1977) 2852–2855, https://doi.org/10.1139/v77-396.

[33] (a) H. Raissi, I. Jamaoui, R. Goumont, T. Boubaker, Kinetic studies on S_NAr reactions of substituted benzofurazan derivatives: quantification of the electrophilic reactivities and effect of amine nature on reaction mechanism, Int. J. Chem. Kinet. 49 (2017) 835–846, https://doi.org/10.1002/kin.21131.I;
(b) T. Jamaoui, Boubaker R. Goumont, Nonlinear Brønsted and Hammett correlations associated with reactions of 4-chloro-7-nitrobenzofurazan with anilines in dimethyl sulfoxide solution, Int. J. Chem. Kinet. 45 (2013) 152–160, https://doi.org/10.1002/kin.20751.

[34] (a) M. Rammah, F. Mahdhaoui, S. Ayachi, T. Boubaker, Exploring the reactivity of benzotriazole derivatives: mayr's approach and density functional theory analysis, J. Mol. Struct. 1247 (2022) 131310, https://doi.org/10.1016/j.molstruc.2021.131310;
(b) A. Laouiti, F. Couty, J. Marrot, T. Boubaker, M.M. Rammah, M.B. Rammah, G. Evano, Exploring the anionic reactivity of ynimines, useful precursors of metalated ketenimines, Org. Lett. 16 (2014) 2252–2255, https://doi.org/10.1021/ol500749h.

[35] H. Ayachi, H. Raissi, F. Mahdhaoui, T. Boubaker, Electrophilic reactivities of 7-L-4-nitrobenzofurazans in σ-complexation processes: kinetic studies and structure-reactivity relationships, Int. J. Chem. Kinet. 52 (2020) 655–668, https://doi.org/10.1002/kin.21390.

[36] H.A. Aref, I. Salama, S.M. Aboukhatwa, M.A. Helal, S.M. Kishk, M.S. Elgawish, 4-Azido-7-nitrobenzoxadiazole as innovative clickable fluorescence probe for trace and selective quantification of ethinylestradiol in human plasma, Luminescence 38 (2023) 1848–1856, https://doi.org/10.1002/bio.4571.

[37] I. Chérif, H. Raissi, K. Abiedh, B. Gassoumi, M.T. Caccamo, S. Magazu, A.H. Said, F. Hassen, T. Boubaker, S. Ayachi, Exploration of intramolecular charge transfer in para-substituted nitrobenzofurazan: experimental and theoretical analyses, Spectrochim. Acta Mol. Biomol. Spectrosc. 301 (2023) 122939, https://doi.org/10.1016/j.saa.2023.122939.

[38] S. El Behi, S. Ayachi, S. Znaidia, Computational modeling for the design of new fluorescent organic compounds based on both diketopyrrolopyrrole and nitrobenzofurazan moieties, J. Mol. Liq. 360 (2022) 119550, https://doi.org/10.1016/j.molliq.2022.119550.

[39] M. Kurt, P.C. Babu, N. Sundaraganesan, M. Cinar, M. Karabacak, Molecular structure, vibrational, UV and NBO analysis of 4-chloro-7-nitrobenzofurazan by DFT calculations, Spectrochim. Acta Mol. Biomol. Spectrosc. 79 (2011) 1162–1170, https://doi.org/10.1016/j.saa.2011.04.037.

[40] M.J. Frisch, et al., Gaussian 09, Revision A.01, Gaussian, Inc., Wallingford, 2009.

[41] A.D. Becke, Density-functional thermochemistry. III. The role of exact exchange, J. Chem. Phys. 98 (1993) 5648–5652, https://doi.org/10.1063/1.464913.

[42] S. Ayachi, S. Ghomrasni, M. Bouachrine, M. Hamidi, K. Alimi, Structure-property relationships of soluble poly (2, 5-dibutoxyethoxy-1, 4-phenylene-alt-2, 5-thienylene)(PBuPT) for organic-optoelectronic devices, J. Mol. Struct. 1036 (2013) 7–18, https://doi.org/10.1016/j.molstruc.2012.09.050.

[43] S. Hajaji, R. Zaier, S. Ayachi, Difluorinated cyclopentadithiophene derivatives for green emitters in organic light-emitting diodes: a theoretical investigation, J. Phys. Chem. Solid. 156 (2021) 110170, https://doi.org/10.1016/j.jpcs.2021.110170.

[44] M. Govindarajan, S. Periandy, K. Carthigayen, FT-IR and FT-Raman spectra, thermo dynamical behavior, HOMO and LUMO, UV, NLO properties, computed frequencyestimation analysis and electronic structure calculations on α-bromotoluene, Spectrochim. Acta, Part A 97 (2012) 411–422, https://doi.org/10.1016/j.saa.2012.06.028.

[45] V. Mishra, A. Raghuvanshi, A.K. Saini, S.M. Mobin, Anthracene derived dinuclear gold (I) diacetylide complexes: synthesis, photophysical properties and supramolecular interactions, J. Org. Chem. 813 (2016) 103–109, https://doi.org/10.1016/j.jorganchem.2016.04.013.

[46] M. Cinar, A. Coruh, M. Karabacak, UV-vis FT-IR, ^{1}H and ^{13}C NMR spectra and the equilibrium structure of organic dye molecule disperse red 1 acrylate: a combined experimental and theoretical analysis, Spectrochim. Acta, Part A 83 (2011) 561–569, https://doi.org/10.1016/j.saa.2011.09.003.

[47] M.H. Jamróz, Vibrational energy distribution analysis (VEDA): scopes and limitations, Spectrochim. Acta, Part A 114 (2013) 220–230, https://doi.org/10.1016/j.saa.2013.05.096.

[48] T.T. Adejumo, N.V. Tzouras, L.P. Zorba, D. Radanovi, A. Pevec, S. Grubiši, D. Mitic, K.K. Andelkovic, G.C. Vougioukalakis, B. Cobeljic, I. Turel, Synthesis, characterization, catalytic activity, and DFT calculations of Zn(II) hydrazone complexes, Molecules 25 (2020) 4043, https://doi.org/10.3390/molecules25184043.

[49] B. Abdelaziz, I. Chérif, B. Gassoumi, S. Patanè, S. Ayachi, Linear and nonlinear optical responses of nitrobenzofurazan-sulfide derivatives: DFT-QTAIM investigation on twisted intramolecular charge transfer, J. Phys. Chem. A (2023), https://doi.org/10.1021/acs.jpca.3c04277.

[50] N. Latelli, S. Zeroual, N. Ouddai, M. Mokhtari, I. Ciofini, Reactivity of nitrobenzofurazan towards nucleophiles: insights from DFT, Chem. Phys. Lett. 461 (2008) 16–20, https://doi.org/10.1016/j.cplett.2008.06.071.

[51] S.F. Boys, F. Bernardi, The calculation of small molecular interactions by the differences of separate total energies. Some procedures with reduced errors, Mol. Phys. 19 (1970) 553–566, https://doi.org/10.1080/00268977000101561.

[52] D. Jayatilaka, S.K. Wolff, D.J. Grimwood, J.J. McKinnon, M.A. Spackman, CrystalExplorer: a tool for displaying Hirshfeld surfaces and visualizing intermolecular interactions in molecular crystals, Acta Crystallogr. A62 (2006) s90, https://doi.org/10.1107/s0108767306098199.

[53] T. Lu, F. Chen, Multiwfn: a multifunctional Wavefunction analyzer, J. Comput. Chem. 33 (2012) 580–592, https://doi.org/10.1002/jcc.22885.

[54] M. Kurt, P.C. Babu, N. Sundaraganesan, M. Cinar, M. Karabacak, Molecular structure, vibrational, UV and NBO analysis of 4-chloro-7-nitrobenzofurazan by DFT calculations, Spectrochim. Acta Mol. Biomol. Spectrosc. 79 (2011) 1162–1170, https://doi.org/10.1016/j.saa.2011.04.037.

[55] D. Vichard, L.J. Alvey, F. Terrier, 4-Chloro-7-nitrobenzofurazan as a Diels–Alder reagent. A facile access to highly functionalized naphthofurazans, Tetrahedron Lett. 42 (2001) 7571–7574, https://doi.org/10.1016/S0040-4039(01)01613-6.

[56] O. Noureddine, S. Gatfaoui, S.A. Brandan, A. Sagaama, H. Marouani, N. Issaoui, Experimental and DFT studies on the molecular structure, spectroscopic properties, and molecular docking of 4-phenylpiperazine-1-ium dihydrogen phosphate, J. Mol. Struct. 1207 (2020) 127762, https://doi.org/10.1016/j.molstruc.2020.127762.

[57] T. Ben Issa, A. Sagaama, N. Issaoui, Computational study of 3-thiophene acetic acid: molecular docking, electronic and intermolecular interactions investigations, Comput. Biol. Chem. 86 (2020) 107268, https://doi.org/10.1016/j.compbiolchem.2020.107268.

[58] E. Scrocco, J. Tomasi, The electrostatic molecular potential as a tool for the interpretation of molecular properties, in: New Concepts II, Springer, Berlin, Heidelberg, 1973, pp. 95–170, https://doi.org/10.1007/3-540-06399-4_6, 42.

[59] P. Politzer , M.C. Concha , J.S. Murray , Density functional study of dimers of dimethylnitramine, Int. J. Quant. Chem. 80 (20 0 0) 184-192. https://doi.org/10.1002/1097-461X(2000)80:2<184::AID-QUA12>3.0.CO;2-O.

[60] I. Chérif, H. Raissi, K. Abiedh, B. Gassoumi, M.T. Caccamo, S. Magazu, A. Haj Said, F. Hassen, T. Boubaker, S. Ayachi, Computational studies on optoelectronic and nonlinear optical properties of para-substituted nitrobenzofurazan compound, Mater. Today Commun. 35 (2023) 106133, https://doi.org/10.1016/j.mtcomm.2023.106133.

[61] I. Chérif, H. Raissi, K. Abiedh, B. Gassoumi, M.T. Caccamo, S. Magazu, A. Haj Said, F. Hassen, T. Boubaker, S. Ayachi, Photophysical and nonlinear optical properties of para-substituted nitrobenzofurazan: a comprehensive DFT investigation, J. Photochem. Photobiol., A: Chem (2023) 114850, https://doi.org/10.1016/j.jphotochem.2023.114850.

[62] K. Wolinski, J.F. Hilton, P. Pulay, Efficient implementation of the gauge-independent atomic orbital method for NMR chemical shift calculations, J. Am. Chem. Soc. 112 (1990) 8251–8260, https://doi.org/10.1021/ja00179a005.

[63] M.B. Stojanović, Can variations of ^{1}H NMR chemical shifts in benzene substituted with an electron-accepting (NO_2)/donating (NH_2) group be explained in terms of resonance effects of substituents? Chem.–Asian J. 13 (2018) 877–881, https://doi.org/10.1002/asia.201800137.

[64] M. Lammert, S. Bernt, F. Vermoortele, D.E. De Vos, N. Stock, Single-and mixed-linker Cr-MIL-101 derivatives: a high-throughput investigation, Inorg. Chem. 52 (2013) 8521–8528, https://doi.org/10.1021/ic4005328.

[65] F.S. Mjalli, M. Al-Azzawi, Aliphatic amino acids as possible hydrogen bond donors for preparing eutectic solvents, J. Mol. Liq. 330 (2021) 115637, https://doi.org/10.1016/j.molliq.2021.115637.

[66] D. Philip, G. Aruldhas, SERS spectra of 2-aminophenol in silver colloids, J. Solid State Chem. 116 (1995) 427–431, https://doi.org/10.1006/jssc.1995.1236.

[67] M. Chaabene, S. Agren, J. El-Haskouri, A. Rahman Allouche, L. Mohamede, R. Ben Chaâbane, M.H. Baouab, Spectroscopic characterization and binding interaction of heavy metal onto the surface receptor of the azobenzene: DFT and experimental approach, J. Mol. Struct. 1244 (2021) 130962, https://doi.org/10.1016/j.molstruc.2021.130962.
[68] A.D. Mašulović, J.M. Lađarević, A.M. Ivanovska, S.L. Stupar, M.M. Vukčević, M.M. Kostić, D.Ž. Mijin, Structural insight into the fiber dyeing ability: pyridinium arylazo pyridone dyes, Dyes Pigments 195 (2021) 109741, https://doi.org/10.1016/j.dyepig.2021.109741.
[69] M. Kurt, S. Okur, S. Demic, J. Karpagam, N. Sundaraganesan, Synthesis and Raman spectroscopic investigation of a new self-assembly monolayer material 4-[N-phenyl-N-(3-methylphenyl)-amino]-benzoic acid for organic light-emitting devices, J. Raman Spectrosc. 42 (8) (2011) 1682–1689, https://doi.org/10.1002/jrs.2910.
[70] S.J. Pradeepa, N. Sundaraganesan, Spectroscopic and molecular structure investigations of 9-vinylcarbazole by DFT and ab initio method, Spectrochim. Acta, Part A 136 (2015) 690–699, https://doi.org/10.1016/j.saa.2014.09.083.
[71] L. Kahovec, W.F. Kohlrausch, Studien zum Raman-Effekt, Z. Phys. Chem. 48 (1941) 7–11, https://doi.org/10.1515/zpch-1941-4803.
[72] B. Gassoumi, A. Mehri, H. Hammami, M.E. Castro, A. Karayel, S. Özkınalı, F.J. Melendez, L. Nouar, F. Madi, H. Ghalla, R.B. Chaabane, H. Ben Ouada, Spectroscopic characterization, host-guest charge transfer, Hirshfeld surfaces, AIM-RDG and ELF study of adsorption and chemical sensing of heavy metals with new derivative of Calix [4]quinone: a DFT-D3 computation, Mater. Chem. Phys. 278 (2022) 125555, https://doi.org/10.1016/j.matchemphys.2021.125555.
[73] E. Katlenok, M.L. Kuznetsov, N.A. Semenov, N.A. Bokach, V.Y. Kukushkin, A new look at the chalcogen bond: π-Hole-based chalcogen (Se, Te) bonding which does not include a σ-hole interaction, Inorg. Chem. Front. 10 (2023) 3065–3081, https://doi.org/10.1039/D3QI00087G.
[74] M. Doust Mohammadi, H.Y. Abdullah, K.W. Qadir, A. Suvitha, Theoretical investigation of intermolecular interactions between CNT, SiCNT and SiCGeNT nanomaterials with vinyl chloride molecule: a DFT, NBO, NCI, and QTAIM study, Diam. Relat. Mater. 131 (2023) 109602, https://doi.org/10.1016/j.diamond.2022.109602.
[75] R.F.W. Bader, Atoms in Molecules: A Quantum Theory, Oxford University Press, Oxford, New York, 1994.
[76] R. Bianchi, G. Gervasio, D. Marabello, Experimental electron density analysis of $Mn_2(CO)_{10}$: metal -metal and metal ligand bond characterization, Inorg. Chem. 39 (2000) 2360–2366, https://doi.org/10.1021/ic991316e.
[77] B. Gassoumi, M. Echabaane, F.E. Ben Mohamed, L. Nouar, F. Madi, A. Karayel, H. Ghalla, M.E. Castro, F.J. Melendez, S. Özkınalı, A. Rouis, R. Ben Chaabane, Azo-methoxy-calix[4]arene complexes with metal cations for chemical sensor applications: characterization, QTAIM analyses and dispersion-corrected DFT-computations, Spectrochim. Acta, Part A 264 (2022) 120242, https://doi.org/10.1016/j.saa.2021.120242.
[78] A. Ramalingam, A.R. Guerroudj, S. Sambandam, A. Kumar, R. Krishnamoorthy, N. Boukabcha, A. Chouaih, M. Elayaperumal, Synthesis, vibrational spectra, Hirshfeld surface analysis, DFT calculations, and in silico ADMET study of 3-(2-chloroethyl)-2,6-bis(4-fluorophenyl)piperidin-4-one: a potent anti-Alzheimer agent, J. Mol. Struct. 1269 (2022) 133845, https://doi.org/10.1016/j.molstruc.2022.133845.
[79] A. Boughougal, R. Kadri, M. Kadri, J.B. Tommasino, G. Pilet, A. Messai, D. Luneau, Novel copper (II) and zinc (II) complexes with enrofloxacin and oxolinic acid: synthesis, characterization, Hirshfeld surface and DFT/CAM-B3LYPD3BJ studies: NBO, QTAIM and RDG analysis, J. Mol. Struct. 1282 (2023) 135141, https://doi.org/10.1016/j.molstruc.2023.135141.
[80] M. Saidj, A. Djafri, R. Rahmani, N.E.H. Belkafouf, N. Boukabcha, A. Djafri, A. Chouaih, Molecular structure, experimental and theoretical vibrational spectroscopy, (HOMO-LUMO, NBO) investigation, (RDG, AIM) analysis, (MEP, NLO) study and molecular docking of ethyl-2-[4-ethyl-5-(quinolin-8-yloxyMethyl)-4H-1,2,4-Triazol-3-yl] sulfanyl acetate, Polycycl. Aromat. Comp. 43 (2023) 2152–2176, https://doi.org/10.1080/10406638.2022.2039238.
[81] M.J. Pramila, D.A. Dhas, I.H. Joe, S. Balachandran, G. Vinitha, Structural insights, spectral, fluorescence, Z-scan, C-H…O/N-H…O hydrogen bonding and AIM, RDG, ELF, LOL, FUKUI analysis, NLO activity of N-2(Methoxy phenyl) acetamide, J. Mol. Struct. 1272 (2023) 134140, https://doi.org/10.1016/j.molstruc.2022.134140.
[82] M. Thirunavukkarasu, P. Prabakaran, A. Saral, N.S. Alharbi, S. Kadaikunnan, A.S. Kazachenko, S. Muthu, Molecular level solvent interaction (microscopic), electronic, covalent assembly (RDG, AIM & ELF), ADMET prediction and anti-cancer activity of 1-(4-Fluorophenyl)-1-propanone): cytotoxic agent, J. Mol. Liq. 380 (2023) 121714, https://doi.org/10.1016/j.molliq.2023.121714.
[83] S. Sundaram, V.N. Vijayakumar, V. Balasubramanian, Electronic and structure conformational analysis (HOMO-LUMO, MEP, NBO, ELF, LOL, AIM) of hydrogen bond binary liquid crystal mixture: DFT/TD-DFT approach, Comput. Theo. Chem. 1217 (2022) 113920, https://doi.org/10.1016/j.comptc.2022.113920.
[84] A.D. Becke, K.E. Edgecombe, A simple measure of electron localization in atomic and molecular systems, J. Chem. Phys. 92 (1990) 5397–5403, https://doi.org/10.1063/1.458517.
[85] L.R. Domingo, M. Ríos-Gutiérrez, A molecular electron density theory study of the reactivity of azomethine imine in [3+2] cycloaddition reactions, Mol 22 (2017) 750, https://doi.org/10.3390/molecules22050750.
[86] J.D.D. Tarika, X.D.D. Dexlin, S. Madhankumar, D.D. Jayanthi, T.J. Beaula, Tuning the computational evaluation of spectroscopic, ELF, LOL, NCI analysis and molecular docking of novel anti COVID-19 molecule 4-dimethylamino pyridinium 3, 5-dichlorosalicylate, Spectrochim. Acta, Part A 259 (2021) 119907, https://doi.org/10.1016/j.saa.2021.119907.
[87] V.S. Jeba Reeda, V. Bena Jothy, Vibrational spectroscopic, quantum computational (DFT), reactivity (ELF, LOL and Fukui), molecular docking studies and molecular dynamic simulation on (6-methoxy-2-oxo-2H-chromen-4-yl) methyl morpholine-4-carbodithioate, J. Mol. Liq. 371 (2023) 121147, https://doi.org/10.1016/j.molliq.2022.121147.